HELSINKI UNIVERSITY OF TECHNOLOGY
Faculty of Electronics, Communications and Automation

Riku Kokko

DEVELOPMENT OF AN ATMOSPHERIC CORRECTION CODE FOR REMOTE SENSING OF WATER QUALITY

Thesis submitted for examination for the degree of Master of Science in Technology

Espoo 24.11.2008

Thesis supervisor:

Professor Martti Hallikainen

Thesis instructor:

Docent Jouni Pulliainen

TEKNILLINEN KORKEAKOULU

DIPLOMITYÖN TIIVISTELMÄ

Tekijä: Riku Kokko

Työn nimi: Ilmakehäkorjauskoodin kehitys vedenlaadun kaukokartoitukseen

Päivämäärä: 24.11.2008 Kieli: Englanti Sivumäärä: 10+74

Tiedekunta: Elektroniikan, tietoliikenteen ja automaation tiedekunta

Professuuri: Avaruustekniikka Koodi: S-92

Valvoja: Professori Martti Hallikainen

Ohjaaja: Dosentti Jouni Pulliainen

Tässä diplomityössä on kehitetty ilmakehäkorjausohjelma MERIS-satelliittidatalle. Ilmakehäkorjaus tarkoittaa maanpinnan reflektanssin arvioimista ilmakehän yläpuolella mitatun radianssin perusteella. Diplomityössä luotu MATLAB-ohjelma käyttää 6SV-säteilynkulkumallia yhdessä ilmakehän satelliittimittausten kanssa. Ohjelma syöttää 6SV-säteilynkulkumalliin aerosolien optisen paksuuden ja otsonin sekä vesihöyryn määrän ilmakehässä. 6SV-säteilynkulkumallilla lasketut ilmakehäkorjausparametrit interopoloidaan kaikiin sateliittikuvan pikseleihin. Lopuksi ilmakehäkorjausohjelma laskee ilmakehäkorjausparametreistä pinnan reflektanssin. Ohjelman arvioimaa vedenpinnan reflektanssia on verrattu sekä pintamittauksiin että MERIS Lakes -prosessoreiden ilmakehäkorjaukseen. MERIS Lakes -prosessoreiden ilmakehäkorjaus todettiin sopivammaksi vedenpinnan reflektanssin määrittämiseen. Jatkossa on kuitenkin mahdollista tutkia, voisiko 6SV-ilmakehäkorjausta käyttää maapinnan reflektanssin määrittämiseen.

Avainsanat: Optinen kaukokartoitus, ilmakehäkorjaus, vedenlaatu, ilmakehä, 6SV-säteilynkulkumalli, MERIS Lakes, Envisat-satelliitti, MERIS-instrumentti, MODIS-instrumentti, OMI-instrumentti

Author: Riku Kokko

Title: Development of an atmospheric correction code for remote sensing of water quality

Date: 24.11.2008 Language: English Number of pages: 10+74

Faculty: Faculty of Electronics, Communications and Automation

Professorship: Space technology Code: S-92

Supervisor: Professor Martti Hallikainen

Instructor: Docent Jouni Pulliainen

In this Master's thesis project an atmospheric correction code using 6SV radiative transfer code and measurements of aerosol optical depth, total column ozone and precipitable water vapor was developed. Here an atmospheric correction means the estimation of surface reflectance based on the measurement of radiance at the top of the atmosphere. The MATLAB code, made in this Master's thesis project, computes atmospheric correction parameters at the points of a grid set on the satellite image. It interpolates the parameters in all pixels of the image. The surface reflectances estimated with the atmospheric correction code has been compared to validation data and to the atmospheric correction of MERIS Lakes processors. The atmospheric correction of MERIS Lakes processors was found to be more suitable for the atmospheric correction of water measurements. However, in the future it is possible to study if the atmospheric correction code, made in this Master's thesis project, could be used for the atmospheric correction of measurements on land area.

Keywords: Optical remote sensing, atmospheric correction, water quality, the atmosphere, 6SV radiative transfer code, MERIS Lakes, Envisat satellite, MERIS instrument, MODIS instrument, OMI instrument

Preface

The this Master's thesis was conducted at Finnish Meteorological Institute's Arctic Reasearch Division during 2008. I would like to thank my instructor Docent Jouni Pulliainen for his advice and guidance during this work. I am also thankful to Professor Martti Hallikainen for accepting to supervise this work and for all his guidelines. Special thanks go to Dr. Tech. Sampsa Koponen from TKK for his guidance, advice and helping hand.

I want to thank my dearest friends for their support and friendship during my studies. Especially Sameena Trina, who kindly helped me to improve the English language in this thesis. I also want to thank the sofa at Joutomiehet for supporting me when my body and mind needed a rest.

Above all, I want to thank my family. Thank you for your support and encouragement during my studies. Thank you for your everlasting love and faith in me. I need you.

Helsinki, 24.11.2008

Riku J. Kokko

Contents

Abstract (in Finnish) ii

Abstract iii

Preface iv

Contents v

Notations viii

Abbreviations x

1 Introduction 1

2 Background theory for the atmospheric correction code 2

2.1 Some basic remote sensing concepts . . . 2

2.2 Interaction between light and the atmosphere . . . 4

2.2.1 Absorption . . . 4

2.2.2 Scattering . . . 6

2.2.3 Refraction . . . 8

2.3 Structure of the atmosphere . . . 10

2.4 Aerosol optical depth . . . 13

2.5 Atmospheric correction methods . . . 14

2.5.1 Image-based methods . . . 14

2.5.2 Empirical method . . . 15

2.5.3 Radiative transfer codes . . . 16

2.5.4 Monte Carlo simulations . . . 18

2.6 6SV radiative transfer code . . . 18

2.6.1 Short algorithm description . . . 19

2.6.2 Absorption modelling . . . 21

2.6.3 Input and output files . . . 22

2.7 The atmospheric correction of MERIS Lakes processors . . . 24

2.8 Remote sensing of water quality . . . 26

2.9 MERIS Lake Water Algorithm . . . 28

3 Instruments and data used in the thesis **29**
3.1 MERIS satellite instrument 29
3.2 MODIS satellite instrument 31
3.2.1 MODIS aerosol product 32
3.2.2 MODIS precipitable water vapor product 34
3.3 OMI satellite instrument and ozone product 35
3.4 Weather station AOD data 35
3.5 Validation data 35

4 Validation of the atmospheric correction code **39**
4.1 The atmospheric correction code based on 6SV radiative transfer code 39
4.2 Atmospheric corrections with and without AOD scaling 40
4.3 Sensitivity of the atmospheric correction for the input parameters . . 43
4.4 The atmospheric correction of MERIS Lakes processors 45
4.5 The effects of atmospheric corrections on the variation of satellite signal 48
4.6 Water parameter estimation with the atmospherically corrected data 50
4.7 Correlation with the in situ data 52
4.8 Atmospheric correction code on land surface 56

5 Summary **57**

References **59**

Appendix A: Documentation of the atmospheric correction code **64**
A.1 ACC.M 64
A.2 READPRODUCT.M 67
A.3 MAP2PIXEL.M 68
A.4 INTERPOLATION_IN_ROI.M 69
A.5 READ_MOD04.M 70
A.6 READ_MOD05.M 71
A.7 READ_OMI.M 71
A.8 READ_HDUMP.M 72
A.9 VALUE_FROM_GRID.M 72
A.10 CM2GCM2.M 73
A.11 WRITE_6S_INPUT.M 73

A.12 READ_6S_OUTPUT.M 73

Appendix B: Scatterplots of in situ radiance reflectance and TOA reflectance 74

Notations

A	area
a	absorption coefficient
a_{gelb}	absorption coefficient of dissolved organic matter (gelbstoff)
a_{pig}	absorption coefficient of phytoplankton pigment
b	scattering coefficient
b_{tsm}	scattering coefficient of total suspended matter
b_b	backscattering coefficient
C_{Chl-a}	chlorophyll-a concentration
C_{TSM}	concentration of total suspended matter
c	speed of light
f	frequency
h	Planck's constant
E	irradiance, spectral irradiance
E	energy
E_d	downwelling irradiance
$E_{in-scat}$	in-scattered irradiance by the atmosphere
E_n	energy of molecule's energy level n
E_S	direct solar irradiance at the top of the atmosphere, solar constant
E_u	upwelling irradiance
E_{sol}^{dir}	direct solar irradiance below the atmosphere
E_λ	spectral irradiance
I	intensity
k	Boltzmann constant
L	radiance, spectral radiance
L_u	upwelling radiance
$L_{u,TOA}$	upwelling radiance at TOA
L_λ	spectral radiance
m_M	molecule's mass
P	power
p	pressure, probability
S	spherical albedo of the atmosphere
T	temperature
T	transmittance
T_g	gaseous transmission
t_d	diffuse transmittance factor
v	velocity
z	altitude
α	extinction coefficient
α	Ångström exponent
β	Ångström coefficient
ΔE	energy change

Δf	frequency change
Δt_n	molecule's excited state's finite natural lifetime
θ	zenith angle
θ_S	sun zenith angle
θ_V	view zenith angle
λ	wavelength of an electromagnetic wave
π	pi
ρ	irradiance reflectance
ρ_a	reflectance of the atmosphere
ρ_{RS}	radiance reflectance, remote sensing reflectance
σ	scattering cross-section
τ	optical depth, optical thickness
τ_A	aerosol optical depth
τ_a	optical depth of aerosol a
τ_g	optical depth of gas g
ϕ_S	sun azimuth angle
ϕ_{S-V}	difference between sun azimuth angle and view azimuth angle
ϕ_V	view azimuth angle
Ω	solid angel

Abbreviations

5S	Simulation of a Satellite Signal in the Solar Spectrum
6S	Second Simulation of a Satellite Signal in the Solar Spectrum
6SV	Second Simulation of a Satellite Signal in the Solar Spectrum - Vector
ASCII	American Standard Code for Information Interchange
AOD	Aerosol optical depth
C2R	Case-2 Regional processor
CCD	Charge-coupled device
DEM	Digital elevation model
ESA	European Space Agency
ECMWF	European Centre for Medium-Range Weather Forecasts
FMI	Finnish Meteorological Institute
HDF	Hierarchical Data Format
HDF4	Hierarchical Data Format 4
HITRAN	High-resolution Transmission molecular Absorption database
ICOL	Improved Contrast between Land and Ocean processor
IFOV	Instantaneous field of view
MERIS	Medium Resolution Imaging Spectral Instrument
MODIS	The Moderate Resolution Imaging Spectroradiometer
MODTRAN	Moderate spectral resolution atmospheric Transmittance algorithm
MOSART	Moderate Spectral Atmospheric Radiance and Transmittance
NASA	National Aeronautics and Space Administration
NASA EOS	NASA Earth Observation System
NCSA	The National Center for Supercomputing Applications
OMI	Ozone Monitoring Instrument
ROI	Region Of the Interest
TKK	Teknillinen korkeakoulu, Helsinki University of Technology
TOA	Top of the atmosphere
TOMS	Total Ozone Mapping Spectrometer
TOSA	Top of the standard atmosphere
SYKE	Suomen ympäristökeskus, Finnish Environment Institute
US	United States
UTC	Universal Time Coordinated
WGS84	World Geodetic System 84

1 Introduction

Remote sensing is a method of taking measurements from a target without making a physical connection with it. Measuring can be done from an airplane or from a satellite, with thousands of kilometers between a measuring device and a target. Typically measuring is done by using electromagnetic radiation. In this work only satellite instruments which sense optical radiation from the Sun are used. However, also other spectral ranges are widely used in remote sensing. They vary from ultraviolet to radio wavelengths.[1]

The origins of many remote sensing techniques are in military applications, but the same techniques can be used in many kinds of environmental applications as well. Remote sensing can be used for the measuring of different surface parameters, e.g. temperature of water, depth of a snow layer, moisture of soil, or it can be used for the measuring of the atmospheric parameters. Remote sensing can also be used for the classification of areas on the Earth surface. One of the biggest advantages of remote sensing is that it allows the investigation of large surface areas or large volumes of the atmosphere in a short period of time. It also makes possible to collect information from locations which could not be investigated in any other way, for example, it may be expensive or dangerous to access these locations in person. Remote sensing also provides information about the target repeatedly. This makes it possible to follow the seasonal changes of the environment.[1]

The atmosphere has an effect on the optical remote sensing measurements. It affects on downwelling radiation from the Sun and on upwelling radiation heading to the satellite sensor. The atmosphere has two main effects on radiation. It absorbs radiation on the absorption lines of its molecules and it scatters radiation. The scattering changes the direction of radiation. It may decrease or increase the amount of radiation reaching the surface or the satellite sensor.[2]

The aim of this Master's thesis is to study the atmospheric correction methods of remotely sensed lake water quality measurements. In remote sensing, the atmospheric correction means the procedure which removes the effects of the atmosphere on the measurement of the target. This basically means that the electromagnetic radiation below the atmosphere is estimated based on the measurement of it at the top of the atmosphere. In this thesis, an atmospheric correction code was developed at Finnish Meteorological Institute. The code uses 6SV radiative transfer code with atmospheric satellite data from MODIS and OMI satellite instruments. The potential end users of the code are FMI, SYKE and TKK.

In Chapter 2, the background theory needed the for the understanding of the atmospheric correction concepts and remote sensing of water quality is given. In Chapter 3, the satellite and the validation data used in this thesis are described. In Chapter 4, the atmospheric correction code based on the 6SV radiative transfer code is briefly described. The surface reflectance estimated with it is compared to the validation data and to the surface reflectance estimated with the atmospheric correction of MERIS Lakes processors. Finally in Chapter 5, the final conclusions are made.

2 Background theory for the atmospheric correction code

2.1 Some basic remote sensing concepts

Observation geometry for optical remote sensing

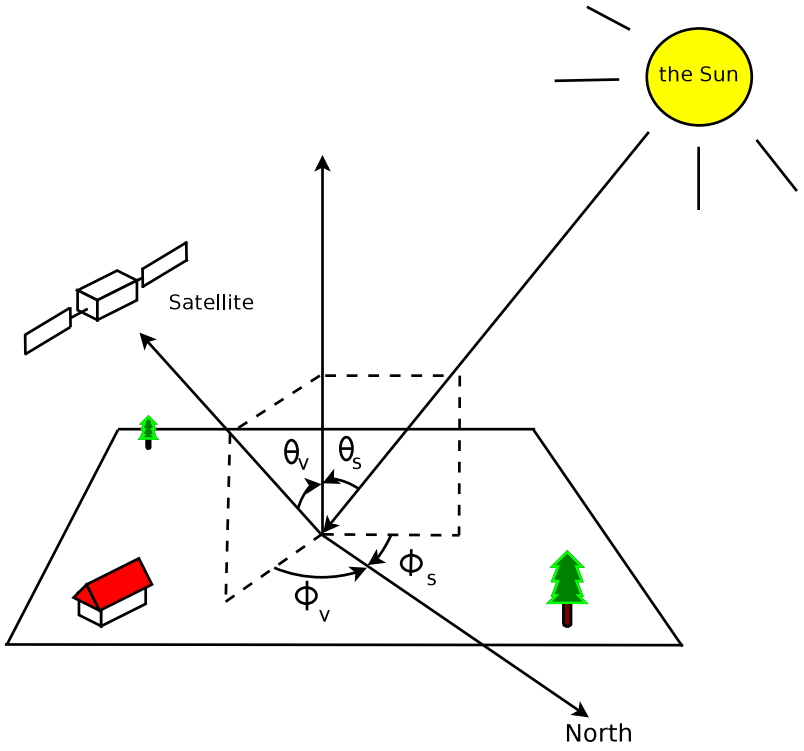

Figure 1: The observation geometry of optical remote sensing.

The geometry for optical remote sensing is presented in Figure 1. The sun zenith angle θ_S is the angle between the local normal and the vector pointing to the Sun from the target. The view zenith angle θ_V is the angle between the local normal and the vector pointing to the satellite sensor from the target. The sun azimuth angle ϕ_S is the angle between north direction and the projection to the ground of the vector pointing to the Sun from the target. Similarly, the view azimuth angle ϕ_V is the angle between the north direction and the projection to the ground of the vector pointing to the satellite from the target. [3]

Radiance

Radiance describes the total power of radiation P, which comes from the area of the source A and falls into solid angle Ω in the specified direction [4]

$$L = \frac{P}{A \cdot \Omega \cdot cos(\theta)}, \tag{1}$$

where θ is the angle between normal of A and the specified direction. Spectral radiance is the radiance per wavelength interval of the radiation $\Delta\lambda$. [4]

$$L_\lambda = \frac{P}{A \cdot \Omega \cdot cos(\theta)\Delta\lambda}, \tag{2}$$

From this point on, radiance is actually meant spectral radiance.

Irradiance

Irradiance is defined as the ratio of the total power of radiation P to the area A' to where the it arrives or which it passes. [4]

$$E = \frac{P}{A'} \tag{3}$$

Spectral irradiance is irradiance per the band of the radiation. [4]

$$E_\lambda = \frac{P}{A' \cdot \Delta\lambda} \tag{4}$$

In the following, when irradiance is mentioned, it refers to spectral irradiance. Where the radiance characterizes the power of the source, the irradiance characterizes the energy arriving to the surface. The radiance does not change as the function of the observation distance, but the irradiance decreases when the distance to the source increases.

Reflectance and radiance reflectance

Irradiance reflectance or just reflectance is the ratio of the reflected upwelling irradiance E_u to the incident downwelling irradiance E_d.[5]

$$\rho(\lambda) = \frac{E_u(\lambda)}{E_d(\lambda)} \tag{5}$$

The reflectance is impossible to measure directly with a satellite instrument. The upwelling irradiance is spread to the hemisphere over the target. However, satellite instruments measure the radiation with a small solid angle. It is more convenient

to measure a radiance reflectance (also known as remote sensing reflectance). It is defined as the ratio of the upwelling radiance L_u to the downwelling irradiance [5].

$$\rho_{RS}(\lambda) = \frac{L_u(\lambda)}{E_d(\lambda)} \tag{6}$$

For a perfect Lambertian surface the reflectance can be derived from the radiance reflectance. A perfect Lambertian surface is a surface which reflects all incident irradiance equally to all directions in the hemisphere. The upwelling irradiance of the Lambertian surface equals [5]

$$E_u(\lambda) = \pi L_u(\lambda). \tag{7}$$

By substituting this to Equation (5) we get a new equation for the reflectance of the Lambertian surface.

$$\rho(\lambda) = \frac{\pi L_u(\lambda)}{E_d(\lambda)} \tag{8}$$

Some times, the reflectance of the Lambertian surface is calculated straight from the values at top of the atmosphere. This so called TOA reflectance [2]

$$\rho_{TOA} = \frac{\pi L_{u,TOA}(\lambda)}{cos(\theta_S) E_s(\lambda)}, \tag{9}$$

where $L_{u,TOA}$ is the upwelling radiance at TOA and E_s is the irradiance from the Sun at TOA.

2.2 Interaction between light and the atmosphere

Optical radiation interacts in three basic ways with the atmosphere. When radiation passes the atmosphere, it is absorbed, scattered and refracted by the atmosphere. These three interactions are described in this section. [6]

2.2.1 Absorption

There are three main absorption methods of electromagnetic radiation in the atmosphere. These absorption methods are related to different changes in molecules' energy levels. When a photon is absorbed by a molecule, the photon's energy may lift the molecule's electron to a higher energy level or it may set the molecule to a higher vibration or rotation energy level. These changes in molecule's energy levels are possible only if the photon's energy corresponds to the energy between the two energy levels. This expressed by Planck's law [6]

$$\Delta E = E_n - E_m = hf, \tag{10}$$

where E_n and E_m are different energy levels of the molecule's quantum mode and $E_n > E_n$. The energy of the photon is given by hf, where h is Planck's constant

and f is the frequency of the photon. The atmosphere absorbs frequencies, which satisfies Equation (10) for the atmosphere's molecules. These frequencies are called spectral lines or absorption lines. By comparing photon's energy to the energies of different transition types, it can be seen which transition type dominate at different parts of the spectrum. At ultraviolet and visible range, the electronic transitions are dominant. At infrared spectral range, the vibrational transitions are dominant. At millimeter spectral range, the rotational transitions are dominant. [6]

For a few reasons, spectral lines are not infinitesimally narrow. The first reason can be derived from the Heisenberg uncertainty principle. Because molecule's excited state's finite natural lifetime Δt_n, the energy level can be determined with only a finite accuracy. We get from the finite accuracy of the spectral line [7]

$$\Delta f_n = \frac{\Delta E}{h} \approx \frac{1}{2\pi \Delta t_n} \tag{11}$$

For the typical lifetimes of electronically excited states Δf_n =10 MHz.[6]

Another reason for the spectral line broadening is Doppler shift, caused by the velocity of the molecules. When a molecule is moving with velocity v and it faces a photon moving towards it, the initial frequency of the photon f_0 is shifted by the amount of [6]

$$\delta f = \pm \frac{v}{c} f_0, \tag{12}$$

where c is the speed of light. The minus sign stands for the situation where the particles are moving apart from each other. The same thing happens to the molecule's spectral line. It is shifted according to Equation (12). The atmosphere consists of molecules moving with random velocities (random speeds and directions). The probability that a molecule in a gas at temperature T has a velocity v is proportional to [6]

$$p \sim exp\left[-\frac{m_M v^2}{2kT}\right], \tag{13}$$

where m_M is the molecule mass and k is the Boltzmann constant. From Equation (12) we get the speed of a molecule causing Doppler shift δf.

$$v = \pm \frac{\delta f}{f_0 c} \tag{14}$$

By inserting (14) to (13) and multiplying it with the initial absorption coefficient we get the broadening of absorption coefficient

$$a_D = a_{D0} \cdot exp\left[-\frac{m_M c^2}{2kT}\left(\frac{f - f_0}{f_0}\right)^2\right], \tag{15}$$

where a_{D0} is the absorption coefficient at the initial frequency f_0. Equation (15) describes a Gaussian shaped spectral line with the center at f_0.[6]

In Figure 2 the gaseous transmission of the atmosphere from the top of the atmosphere to the sea level is plotted. The transmission is calculated by using 6SV

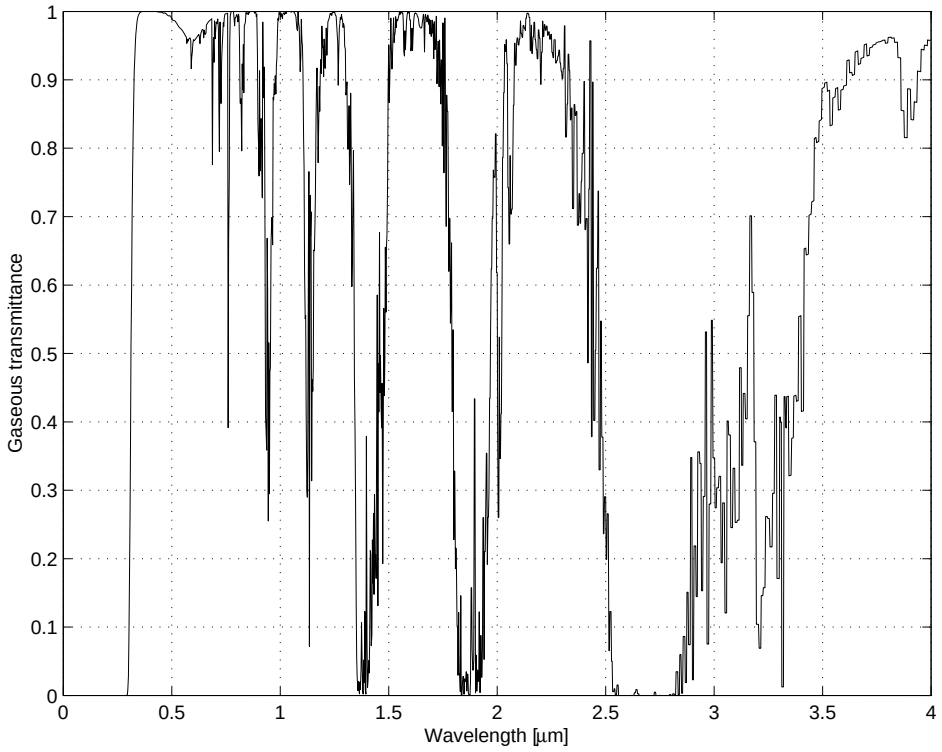

Figure 2: The gaseous transmittance of the atmosphere from the top of the atmosphere to the sea level. The transmittance was simulated with 6SV radiative transfer code with US62 standard atmosphere and with zero view zenith angle.

radiative transfer code with US62 standard atmosphere and nadir view. The gaseous transmission is the transmittance, which takes into account only the effect of the molecular absorption. It is inversely proportional to the absorption coefficient α. In the transmission of the atmosphere the absorption lines can be seen. Also that they are not infinitesimally narrow can be seen.

2.2.2 Scattering

In scattering a photon collides to a molecule or to an aerosol particle. The energy of the photon is not lost, but it is redirected. The scattering properties of a particle is described with scattering cross-section σ. The intensity of the radiation from the scattering particle is defined as [6]

$$I_{scat} = \sigma I_0, \tag{16}$$

where I_0 is the intensity of initial radiation.[6]

Scattering can be divided into three categories. When the scattering particles are small compared to the wavelength of the photon, the scattering is called Rayleigh scattering. It can be shown that the Rayleigh scattering is proportional to λ^{-4} [1]. This means that the ultraviolet and blue light are much more likely scattered

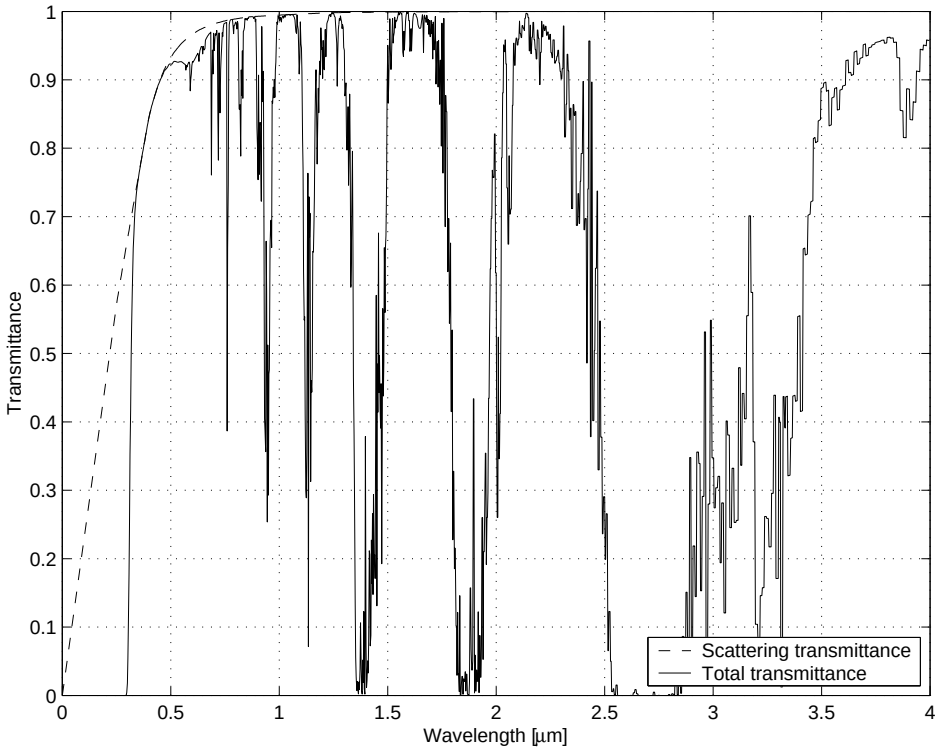

Figure 3: The transmittance caused by the atmospheric scattering of photons away from the view and the total transmittance of the atmosphere from the top of the atmosphere to the sea level. The transmittance was simulated with 6SV radiative transfer code. In the simulation, US62 standard atmosphere and zero view zenith angle were used.

than the red light and the infrared light. If the particle is much bigger than the wavelength, the scattering is called non-selective scattering. In the non-selective scattering the amount of the scattering is independent of the wavelength. The third type of scattering is between the previous cases. It is called Mie scattering and it can be shown to be proportional to λ^{-1}. All in all, scattering has a stronger effect on the shorter wavelengths. This can be seen from the scattering transmittance in Figure 3. The scattering transmittance, simulated with 6SV radiative transmittance code, is the ratio of the electromagnetic flux scattered away from the field of view to the incident electromagnetic power to the atmosphere. The effect of stronger scattering at the shorter wavelengths can also be seen in the blue color of the sky. When we look at the sky away from the Sun, our eyes capture sun photons scattered by the sky. Because the photons at the short wavelengths are more likely to be scattered, our eyes capture more photons from the short wavelengths of the spectrum. Another example of the scattering effect of the atmosphere can be seen after the sun set. After the sun set there is no direct light from the Sun. However, one can still see plenty of light. This light is sun light scattered by the atmosphere. [1] [8]

For the sun-satellite system's radiative transfer the atmospheric scattering has two basic effects. The scattering of the atmosphere affects on the downwelling, solar

irradiance measured below the atmosphere and on the upwelling radiance measured by the satellite at the top of the atmosphere. These two effects are described in Figure 4. The downwelling irradiance measured below the atmosphere does not consist only of the light directly from the Sun but also of light which has been scattered by the atmosphere. This is illustrated with the beam number 2 in the figure. There can be several scattering events for one photon. The solar irradiance below the atmosphere has also the component which has been scattered by the surface and the atmosphere nearby the measurement point of the irradiance. In Figure 4 this is the beam number 3. Also, in this case the scattering may happen several times between the surface and the environment. This light is scattered by the atmosphere and is the sum of beams number 2 and 3. The radiance measured by the satellite sensor does not consist only of the light directly from the IFOV. There is also a component scattered by the atmosphere, in Figure 4 this is beam number 4, as before the beam may scatter several times in the atmosphere. In the irradiance component there is also a component scattered near the IFOV and then scattered by the atmosphere to the sensor, this is beam number 5. Scattering has a great effect on the measurement at the top of the atmosphere reflectance. [2]

2.2.3 Refraction

According to the Fermat's principle, a beam of light takes the path that minimizes the time to reach the target. When the density of the atmosphere varies with altitude, the speed of light varies too. This means that the path of the beam is bent if the incident beam is not perpendicular to the atmosphere. This effect can be seen when the Sun sets down. It is possible to see the Sun even after it is under the horizon. Because of the bending of the path caused by the refraction, the Sun is visible for a few minutes more. [4] [8]

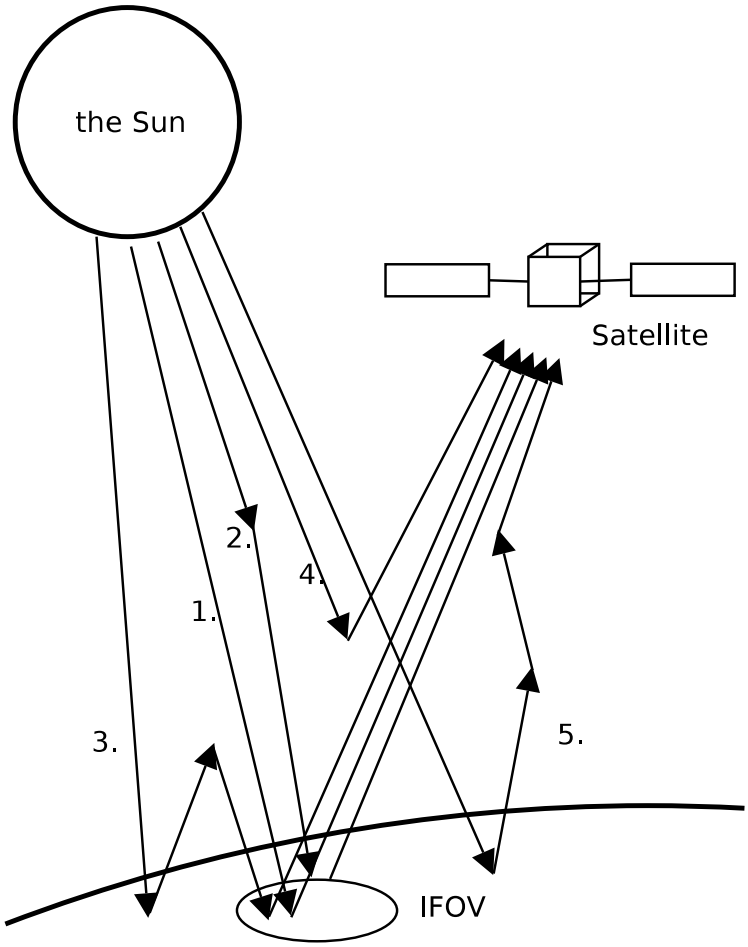

Figure 4: The scattering of light in the atmosphere. Beam number 1 comes directly from the sun and reflects from IFOV to the satellite sensor. Beam 2 is heading outside IFOV before it is scattered by the atmosphere into the IFOV. Beam 3 is reflected upward by an area near IFOV and scattered by the atmosphere into the IFOV. Beam 4 is scattered to the satellite sensor without reaching the surface. Beam 5 is reflected by an area nearby IFOV and then scattered by the atmosphere to the sensor.

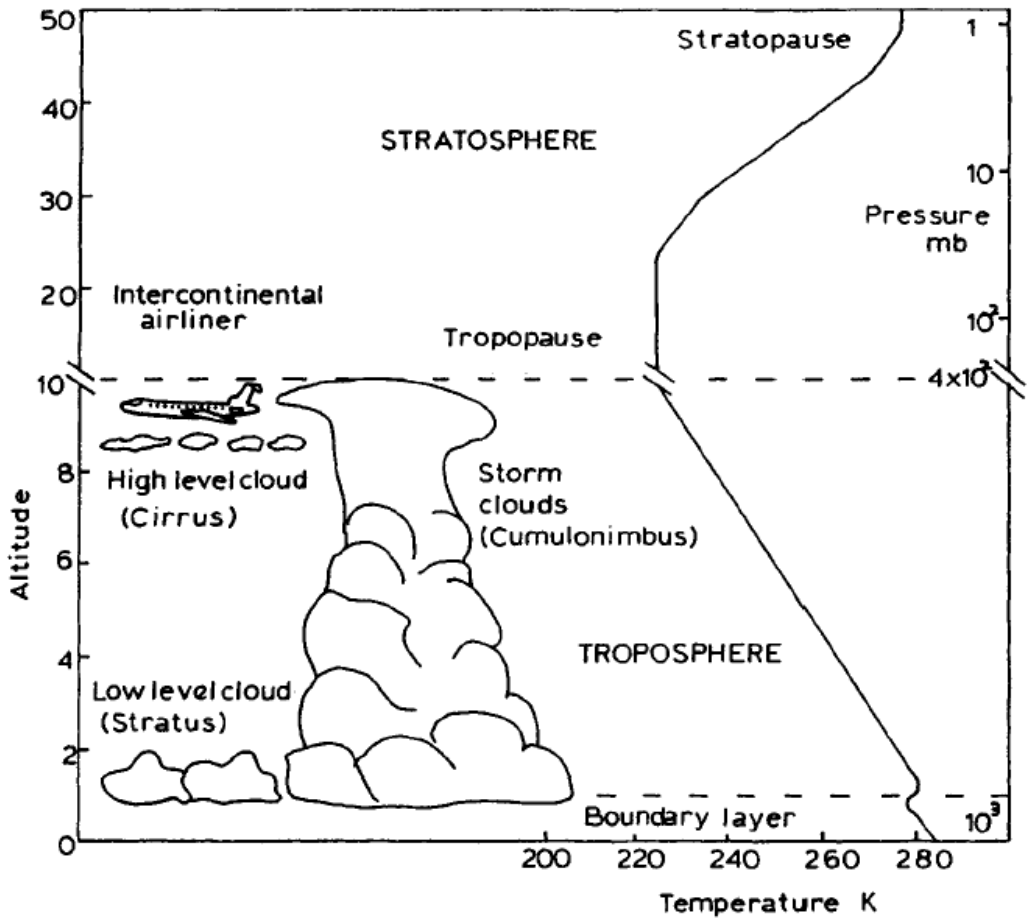

Figure 5: The atmosphere is divided to different spheres according to the direction of the temperature change. The source of figure is [7].

2.3 Structure of the atmosphere

The atmosphere is divided into different layers. These layers are called spheres. In one sphere the temperature change is usually monotonic when we are moving higher. Between the spheres are pauses, where the temperature change turns its direction . The spheres are described in Figure 5. The first sphere from the ground is troposphere. In the troposphere, the temperature decreases until it reaches tropopause where the temperature decrease stops. Near the poles, the tropopause at the altitude of 8 km and in the tropics it is at the altitude of approximately 18 km. Because the temperature decreases in the higher altitudes of troposphere, warm air will rise up. This causes air streams and mixing of the air. The troposphere contains approximately 75% of the atmosphere's mass and contains most of the water vapor and aerosols of the atmosphere. Also most of the clouds are in the troposphere. In this layer most of the variability of conditions takes place, which leads to the weather changes. [8] [7]

The part of the troposphere where a surface has a strong effect on the behavior of the

air is called boundary layer. It reaches from the surface of the Earth to around 2 km altitude. The maximum altitude vary significantly depending on the atmospheric conditions. In the boundary layer, the atmosphere has much vertical, turbulent winds and it is not statistically stable. The turbulence winds occur when the winds meet the shapes of the terrain. The type of the terrain affects the variation of the wind; so that the more rough the surface is , the more variation there is (e.g. the surface of a city vs. the smooth surface of a lake). [9] [8] [7]

The temperature decreases monotonically in the troposphere, but when we rise above the troposphere and tropopause, the decreasing stops and the temperature starts to increase. This layer is called stratosphere. Temperature increases in the stratosphere until the stratospause, is reached at 50 km altitude. The temperature increase is caused by molecules' absorption of the short wavelengths of the solar radiation. The ozone molecule, O_3, has an important role in this. First oxygen molecule, O_2, is decomposed to oxygen atoms, O, by the shortwave solar radiation. These free oxygen atoms and oxygen molecules easily compose ozone, O_3. The ozone molecules absorbs the ultraviolet radiation of the Sun. The ultraviolet radiation decomposes ozone to a oxygen atom and a molecule. After this, the reaction chain starts again. The reaction chain causes ozone layer between the altitudes of 25 km and 30 km, where the rate of ozone compositions and decompositions are equal. [8] [7]

Vertical streams of air are weak in the stratosphere. This is because of the temperature increases on higher altitudes. Warm air will rise only until it meets air with the same temperature. This makes the stratosphere more stable than the troposphere. The stratosphere is relative cloud free and less turbulent than the troposphere. [7]

Layers up from the stratospause are very sparse. These are mesosphere, thermosphere, ionsphere and exosphere. These layers are stable and they do not have a strong effect on the optical radiative transfer. The ionosphere reflects electromagnetic waves at radio frequencies. [7]

Atmospheric pressure and density decrease quickly with the height above the Earth. This is because gravity pulls atmosphere's molecules towards the Earth. The distribution of the density is roughly exponential. Below 100 km, it is 99.99997 % of atmosphere's mass. All remote sensing satellites see through practically the whole atmosphere.

The atmosphere is a mixture of gasses. The compostion of the dry atmosphere is presented in Table 1. Besides the dry part of the atmosphere, there is water vapor and aerosols as well. For the solar radiation, the principal absorbing gases are water vapor, carbon dioxide, oxygen and ozone [10]. The distributions of carbon dioxide and oxygen are relatively constant. The distributions of water vapor, ozone and aerosols depend on the time and location, which makes them important cases for the atmospheric correction. These three are viewed with more detail.

Water vapor is water in the gaseous phase. Because of water's strong electromagnetic properties, water vapor has a great effect on the transmission of the electromagnetic radiation. The density of water vapor decreases exponentally as a function of altitude with decreasing to the fraction of e in 2.5 km [11]. Water vapor is an im-

Table 1: Principal composition of the dry atmosphere [8]. In addition to these substances, there are also water vapor H_2O and aerosols in the atmosphere.

Gas		
Nitrogen	N_2	78.1 %
Oxygen	O_2	20.9 %
Argon	Ar	0.93 %
Carbon dioxide	CO_2	0.035 %
Neon	Ne	0.0018 %
Helium	He	0.0005 %
Methane	CH_4	0.00017 %
Krypton	Kr	0.00011 %
Hydrogen	H_2	0.00005 %
Ozone	O_3	0.000004 %
Nitrous oxide	NO_2	$<$ 0.000004 %

portant parameter to atmospheric corrections because it has strong absorption lines on infrared and microwave regions [10]. The amount of water in the atmosphere is measured with total precipitable water vapor. It is the depth of a water layer on the Earth's surface if all water vapor in an atmospheric column above the surface would precipitate [12]. Typical values for the total precipitable water vapor are between 0 cm and 7 cm.

As described before, ozone absorbs harmfull ultraviolet light. Ozone absorbs all wavelengths shorter than 300 nm. It lies in a layer from 25 km to 30 km but its distribution is highly variable. The amount of ozone in the atmosphere column is measured in Dobson units. The Dobson unit is the depth of a pure ozone layer on the Earth's surface, if all ozone above the surface were compressed to the standard pressure and temperature. The thickness of the layer is measured in hundredths of a millimeter. A typical value of the Dobson unit in the atmosphere is 300 DU, which corresponds of 3 mm layer of ozone on the surface [13]. Some times cm $\cdot$ atm is used instead of the Dobson unit. 1 cm $\cdot$ atm equals 1000 DU. [14]

Aerosols are solid or liquid particles in a gas. Typical atmospheric aerosols are dust, sea salt, volcanic and industrial ash. The sizes of the particles vary from nanometers to tens of micrometers. They can be found from the two lowest atmospheric layers, troposphere and stratosphere. The concentration of aerosols decreases with the altitude. For the atmospheric correction, aerosols are important because they scatter and absorb electromagnetic waves. The modelling of aerosols is difficult because their size distribution and amount vary with time and location. New aerosols emerge and some leave the atmosphere. New aerosols rise from land and the sea. They may come as industrial combustion products or as soot from volcanos or biomass burning. By the time, aerosols fall down due to the gravitation and rain. Different land types has their own typical aerosol distributions. For example, aerosol distribution in

desert differ from the distribution in coastal areas. The effect of aerosols on the transmission is measured with aerosol optical depth. This concept is described in the next section. [15]

2.4 Aerosol optical depth

Optical depth characterizes how much a material layer attenuates the initial intensity of the radiation I_0 in it. According to Elachi [11], in a thin atmospheric layer D the intensity change is

$$dI = -\alpha I dz \Rightarrow I(z) = I_0 e^{-\alpha z}, \tag{17}$$

where α is the extinction coefficient, z is the altitude and I_0 is the intensity before the arrival to the material layer. After passing the layer the intensity is

$$I(D) = I_0 e^{-\alpha D} \tag{18}$$

The term αD is called optical thickness τ. From (18) we get a relation between the transmittance and the optical thickness.

$$T = e^{-\tau} \tag{19}$$

If the extinction coefficient varies with altitude, the optical thickness of a layer between altitudes z_1 and z_2 at wavelength λ is

$$\tau(\lambda, z_1, z_2) = \int_{z_1}^{z_2} \alpha(\lambda, z) dz. \tag{20}$$

The total optical thickness of the atmosphere from the surface of the Earth to the top of the atmosphere is called optical depth [11].

$$\tau(\lambda) = \int_0^{\infty} \alpha(\lambda, z) dz \tag{21}$$

If a wave propagates with a zenith angle θ in the atmosphere, the optical depth becomes [11]

$$\tau(\theta, \lambda, z) = \frac{\tau(\lambda, z)}{cos(\theta)}. \tag{22}$$

The dry atmosphere is a mixture of gases and aerosols, the total optical depth is the sum of molecular optical depths $\tau_g(\lambda)$ and aerosol optical depths $\tau_a(\lambda)$. [11]

$$\tau = \sum \tau_g(\lambda) + \sum \tau_a(\lambda) \tag{23}$$

The sum of optical depths caused by different types of aerosols is called aerosol optical depth (AOD). When τ is much greater than 1, layer is said to be optically thick. When τ is much smaller than 1, layer is said to be optically thin. A typical value for the total optical depth of the atmosphere at 550 nm is around 0.3, where 0.1 comes from the gaseous transmission and 0.2 from aerosols [1]. The annual-mean

aerosol optical depth is roughly 0.1, but local values can vary considerably from the annual-mean value [16].

The measurements of the aerosol optical depth $\tau_A(\lambda_0)$ can be extended to all wavelengths λ with two empirical formulations. Mostly used formulation is called Ångström law. [17]

$$ln\left(\tau_A(\lambda)\right) = ln\beta - \alpha ln\frac{\lambda}{\lambda_0}, \tag{24}$$

where α and β are empirical parameters, Ångström exponent and Ångström coefficient, respectively. From (24) we also get.

$$\tau_A(\lambda) = \beta\left(\frac{\lambda}{\lambda_0}\right)^{-\alpha} \tag{25}$$

Another method is to use a second order polynomial fit. [17]

$$ln\tau_A(\lambda) = a_0 + a_1 ln\lambda + a_2\left(\ln\lambda\right)^2 \tag{26}$$

It is proposed in [17] that Equation 26 should be used if sufficient number of samples are available to its three degrees of freedom.

2.5 Atmospheric correction methods

In remote sensing, an atmospheric correction means a procedure which removes the effects of the atmosphere on the measurement of the target. This basically means that the electromagnetic radiation below the atmosphere is estimated based on the measurement of it at the top of the atmosphere. Atmospheric correction methods can be divided into three classes: image-based methods, empirical methods and radiative transfer models. In this section the methods are described briefly. In Section 2.6 a radiative transfer code, called 6SV, is described in more detail. Also the atmospheric correction of MERIS Lakes processors, using neural network trained with Monte Carlo simulations, is described in Section 2.7. [18]

2.5.1 Image-based methods

With image-based atmospheric correction methods, it is possible to eliminate the effect of the additional path radiance by assuming that the dark pixels of the satellite image have only an atmospheric scattering component. However, these methods are not capable of taking into account the effects of a varying transmittance or temporal changes in separate pictures. Also the assumption of the additional path radiance does not work on surfaces with low reflectances. Two commonly used image-based methods are a histogram minimum method and a regression method. [18]

In the histogram minimum method, it is assumed that the radiance of a very dark pixel, e.g. water or dark shadow pixel, contains only components scattered from the atmosphere, and the target by itself has zero reflectcance. The radiance of a dark

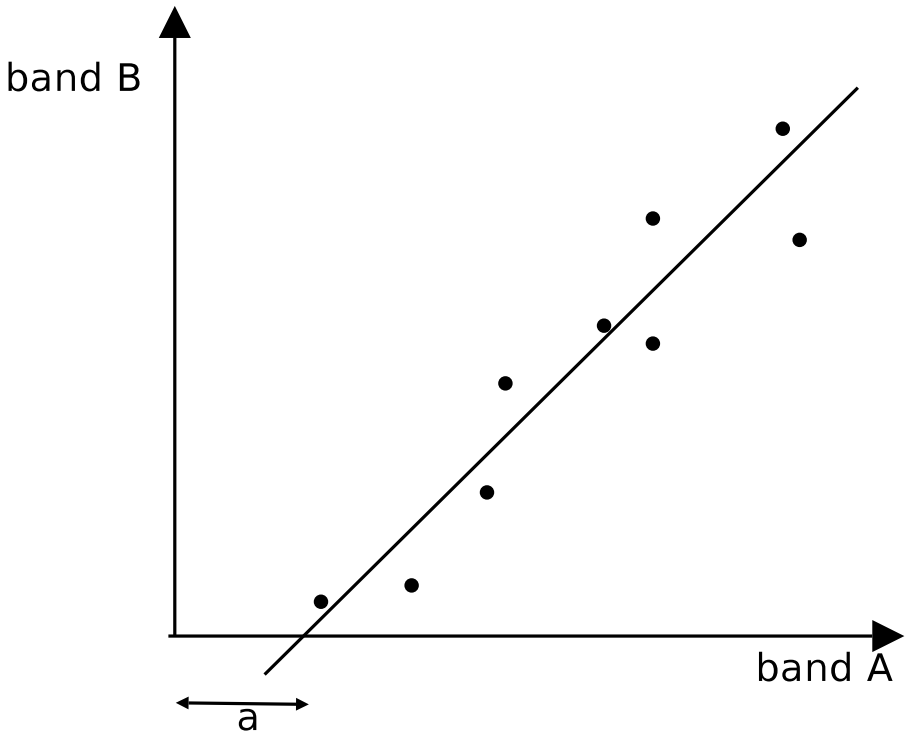

Figure 6: The regression method for the atmospheric correction. Sensor's infrared or near-infrared spectral band B is plotted against the spectral band A to be corrected. A first order polynomial is fitted into the points using a linear regression. The offset on the axis A is used as the estimate of the path radiance for the same channel.

pixel is then subtracted from all other pixels' radiances in the same channel. The atmospheric radiance on the dark pixels of the infra-red and near infra-red channels are very close to zero and the atmospheric correction is not made to these channels. [18]

Another image-based method is the regression method. It is also applicable only to the pictures with dark pixels. Sensor's infrared or near-infrared spectral band B is plotted against the spectral band A to be corrected, as in the Figure 6. A first order polynomial is fitted into the points using linear regression. The offset on the axis A is used as an estimate of the path radiance for the same channel.[18]

2.5.2 Empirical method

An atmospheric correction can also be made using an empirical line method. Two targets are selected, one light and one dark. Their reflectances ρ are measured on the ground. These values are plotted with the radiance L recorded by the satellite sensor as in Figure 7. These two points are connected with a line. The slope k and the interception a of the line are calculated. The slope is an estimate for the atmospheric transmittance and the interception is an estimate for the atmospheric path radiance.

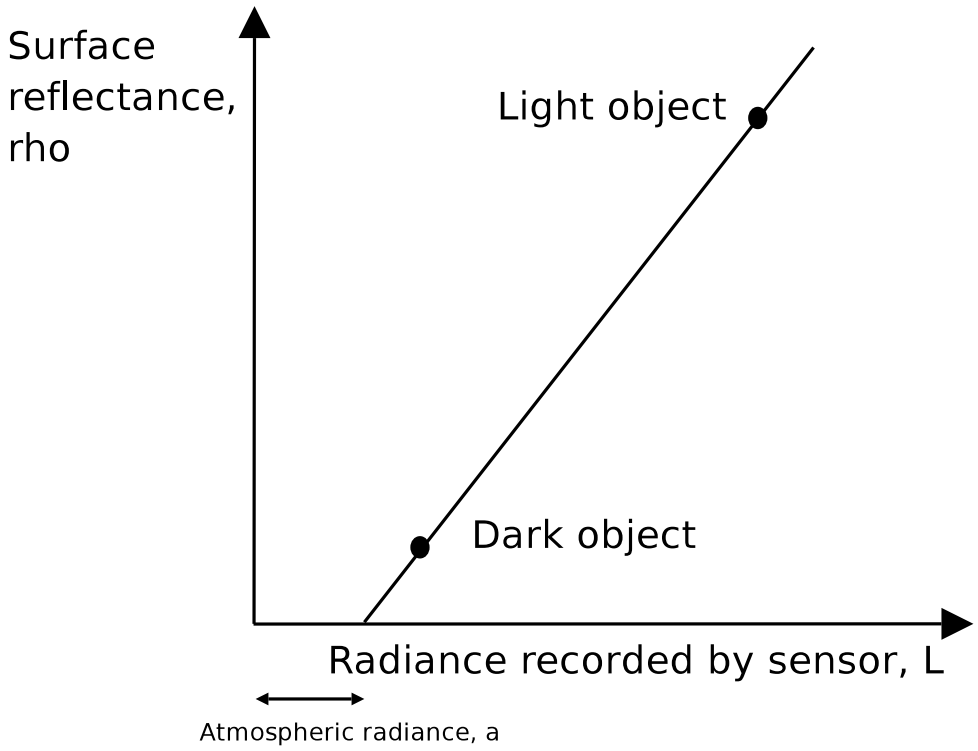

Figure 7: The empirical method for the atmospheric correction. The surface reflectance is measured at light and dark surface. They are plotted with the corresponding satellite measurements. From the line, it is estimated the atmospheric transmittance and the atmospheric path radiance.

By using these, we get a function for all values of the surface reflectance

$$\rho = k(L - a). \tag{27}$$

This equation is computed for all the channels of interest. A shortcoming of the empirical method is that it needs the local reflectance data. [18]

2.5.3 Radiative transfer codes

Radiative transfer codes try to simulate the very complicated transfer process of an electromagnetic wave in the atmosphere. The radiative transfer codes can be used for estimation of the signal at the top of the atmosphere based on the signal measured below the atmosphere. Also, they can be used for the estimation of the signal below the atmosphere based on the signal measured at the top of the atmosphere. In addition to the remote sensing applications, the radiative transfer codes can be used in environmental sciences for studies of clouds and aerosols, in atmospheric photo-chemistry and in military applications for improving the detection of hidden objects, visibility studies and atmospheric transmission calculations for high-energy lasers [19].

The radiative transfer codes need line-of-sight geometry and spectral range as input arguments. Also atmospheric parameters, e.g. AOD, total precipitable water vapor, total column ozone or CO_2 concentration, may be taken as an input to increase the quality of the estimated signal. Operational usage of radiative transfer models for atmospheric correction can be difficult because of the lack of atmospheric parameters needed for the estimation. Because of this, standard atmospheric profiles are often used instead of the measured parameters. This causes loss of accuracy [20].

The radiative transfer codes can be used in a direct sense for solving the signal as mentioned above or in a inverse sense for solving the atmospheric parameters. In the direct problem, the atmospheric parameters are known and the signal is solved at top of the atmosphere or below the atmosphere. In the inverse problem atmospheric parameters are solved based on the measured signal [21]. Aerosol optical depth, AOD, is an important atmospheric parameter, which can be solved in this way from satellite signal. The radiative transfer codes are often used for the calculation of standard reference tables for varying geometrical and atmospheric conditions. The tables are then used for the solving of the direct and inverse problems. The tables connect the signal measured at one end of the atmosphere to the signal at the other end of the atmosphere and to the atmospheric parameters. The tables have discrete values of signals and atmospheric parameters. The discrete values are interpolated to calculate intermediate values if needed.

The radiative transfer codes use different kinds of methods for the simulation of the radiative transfer in the atmosphere, such as Eddington approximation [22], the F_N method [23], the discrete ordinates method [24]-[25], Monte Carlo method [16], the spherical harmonics method [26], line-by-line method and successive order of scattering method [2]. In the following section, some radiative transfer codes are described briefly. In section 2.6, 6SV radiative transfer code is described in more detail. In Section 2.7 the atmospheric correction algorithm of MERIS Lakes processors is described.

MODerate spectral resolution atmospheric TRANsmittance algorithm and computer model, MODTRAN, is a radiative transfer model developed by US Air force research laboratory / Space vehicles division and Spectral sciences Inc. The code can be used for several purposes, including the atmospheric correction. MODTRAN estimates the atmospheric transmittance and the path radiance, which can be used for the estimation of the surface reflectance from the TOA signal. MODTRAN covers spectral region from 0 $cm^{-}1$ radio waves to 50,000 $cm^{-}1$ ultra-violet with spectral resolution of 2 $cm^{-}1$. [31] MODTRAN has been widely used in remote sensing for the estimation of the TOA signal and estimation of the surface signal. The latest public version, MODTRAN4, is available with a $300 fee from `http://www.kirtland.af.mil/library/factsheets/factsheet.asp?id=7915`. The Moderate Spectral Atmospheric Radiance and Transmittance code, MOSART, is a radiative transfer code developed under the funding of the United States Department of Defense. MOSART calculates the atmospheric transmission and radiation in the ultraviolet through the microwave regions. MOSART includes features from other atmospheric correction codes, APART, LOWTRAN and MODTRAN, which

are also developed under the US Department of Defence. MOSART have some additional new features. [32] However, MOSART is not thoroughly tested in the remote sensing community. Also, the documentation of MOSART has not been able to follow the evolution of the software. In this thesis the it was studied if MOSART could be used in the atmospheric correction of MERIS water quality measurements. However, the 6SV radiative transfer code was chosen to atmospheric correction code. It was seen more reliable and easier to use. Other radiative transfer codes used for the atmospheric correction, but not described here, are LOWTRAN [27], ARTEM [29], FASCODE, RT3 and SHARM.

2.5.4 Monte Carlo simulations

In the widest sense, Monte Carlo simulation means any simulation which uses random numbers [33]. The Monte Carlo method can be used to simulate a great number of different mathematical, physical, technical and financial problems. For example in mathematics, the Monte Carlo method can be used for a numerical integration or in the physics for simulations of the nuclear particles' transportation. In remote sensing, the Monte Carlo method can be used for the simulation of photon transportation in the atmosphere. This way synthetic data for the validation of radiative transfer codes can be produced, as was made by Kotchenova et al. in [21]. They used Monte Carlo simulations by Bréon [34]. In his simulation, the radiative transfer in the atmosphere is modelled by simulating a large number of photons transferring from the upper atmosphere to the surface and from there to the satellite sensor. As the result of the simulation we get data, which attache surface reflectance to atmospheric parameters and to TOA reflectance. The data cannot be directly used for the atmospheric correction, but the data can be used for the validation of analytical radiative transfer models. The data can also be used for the training of neural network, which executes the atmospheric correction. Atmospheric correction was made in this way in the atmospheric correction of MERIS Lakes processors, which is described in Section 2.7.

2.6 6SV radiative transfer code

Second Simulation of a Satellite Signal in the Solar Spectrum, 6S, is a FORTRAN code capable for both simulation directions of the satellite signal. It can be used for the estimation of TOA reflectance based on the surface reflectance or it can be used for the estimation of the surface reflectance based on the TOA reflectance. According to Vermote, the main developer of 6S, 6S is one of the most used, rigorously validated and heavily documented radiative transfer codes in the scientific remote sensing community [2]. 6S has been used e.g. in [35], [36] and [14]. It is also used for the computation of the atmospheric correction look-up tables for the MODIS surface reflectance data product [37]. It was also used for the atmospheric correction of lake measurements in [38].

One of the main advances, for example compared to MODTRAN or MOSART, is

that 6S is designed for the atmospheric correction, which makes it simple to use. Also, documentation is much better compared to the MOSART radiative transfer code.

6S is an improved version of Simulation of a Satellite Signal in the Solar Spectrum, 5S, which was developed in 1987 at Laboratoire d'Optique Atmosphérique, University of Lille, France. The improvements of 6S are, the ability to use near-nadir aircraft observations, the accounting for target elevation, non Lambertian surface conditions and three new absorbing species [10]. The development work on the 6S has continued in the United States, in the University of Maryland and MODIS Land surface reflectance science computing faculty. The newest version of 6S was released on May 2005. It is called 6SV, where V refers to a vector. Instead of handling radiance as a scalar, 6SV take also into account the polarization of the electromagnetic wave. The polarization is simulated with the help of four components of Stokes vector. With 6SV, it is also possible to adjust the accuracy of the simulation by changing the number of calculation layers and scattering angels.[2]

6SV assumes cloudless atmosphere. The spectral resolution of 6SV is 2.5 nm. Because of the modelling methods of the atmosphere, 6SV cannot be used for limb observations or on spectral bands with strong absorption bands. The radiative transfer simulation of 6SV can be divided into two parts, simulation of scattering and simulation of absorption. These are described in the following sections.

6SV and three other radiative transfer codes, MODTRAN, RT3, SHRAM have been compared by Kotchenova et al.[21] against the radiative transfer benchmarks, Bréon's Monte Carlo code [34] and Coulson's tabulated values. Coulson's tabulated values represents the complete solution of Rayleigh problem for a molecular atmosphere. These tables give the exact distribution and polarization of the reflected and transmitted light in the atmosphere for a different geometry, surface reflectance and atmospheric conditions [39]. Kotchenova et al. found that the surface reflectance estimated with 6SV gave the best results against the Monte Carlo code. 6SV and RT3 was shown to have the agreement with Coulson's values. 6SV's average difference to the Coulson's values was less than 0.13 %. In [40] Kotchenova et al. compared MODIS Aqua water-leaving reflectances, corrected with 6SV, to in situ reflectances. At 400 nm - 550 nm the difference between the reflectances was under 2 %.

The 6SV code is distributed publicly and without charge by MODIS Land surface reflectance science computing faculty at `http://6s-ltdri.org`. From this web page 6SV manuals and publications can also be found. Also a web interface for 6SV is provided.

2.6.1 Short algorithm description

Here, a short description of atmospheric correction of 6SV is given according to [2]. The description here gives the basic idea of the correction. However, some details are left out. More information of the 6SV algorithm can be found from [10] and [2].

The atmospheric downward transmittance without the effect of absorption can be

divided into two parts. The first part is due to the optical depth of the atmosphere. The direct solar irradiance at the top of the atmosphere E_S is decreased because of the sun zenith angle θ_S and the optical depth of the atmosphere τ. The direct solar irradiance below the atmosphere is [2]

$$E_{sol}^{dir} = \mu_S E_S e^{-\tau/\mu_S}, \tag{28}$$

where $\mu_S = cos(\theta_S)$. The second part of the downward transmittance is due to the in-scattering to the surface. This part takes into account the radiation scattered to the surface from outside the direct direct path. It is noted with diffuse transmittance factor t_d, which is the ratio of the in-scattered irradiance $E_{in-scat}(\theta_S)$ to the direct solar irradiance. [2]

$$t_d(\theta_S) = \frac{E_{in-scat}(\theta_S)}{\mu_S E_S} \tag{29}$$

Thus the downward transmittance due to the direct irradiance and the in-scattering is

$$T(\theta_S) = e^{-\tau/\mu_S} + t_d(\theta_S). \tag{30}$$

The surface target is also illuminated by the radiation which is reflected by the surface near the target and then reflected by the atmosphere to the target. The reflections can occur multiple times. [2]

$$T(\theta_S)[\rho_t S + \rho_t^2 S^2 + ...] \tag{31}$$

ρ_t is the reflectance of the target and S is the spherical albedo of the atmosphere. The total irradiance is

$$E_d = T(\theta_S)[1 + \rho S + \rho^2 S^2 + ...]. \tag{32}$$

As the sum of geometric series we get

$$E_d = T(\theta_S)/[1 - \rho_t S]. \tag{33}$$

The radiance at satellite level can be divided into three parts, the direct radiance from the surface, the radiance from the environment around the target and the radiance reflected by the atmosphere. The first part results from the solar radiation reflected by the surface and directly transmitted from the surface to the sensor zenith angle θ_V. The transmittance for this radiation is [2]

$$\mu_V e^{-\tau/\mu_V}, \tag{34}$$

where $\mu_V = cos(\theta_V)$ and θ_V is the view zenith angle. The second part is reflected by the environment near the target and then reflected by the atmosphere to the sensor. This radiation is noted with t_d, as it was noted with the downwelling scattered radiation. The upward atmospheric transmittance becomes [2]

$$T(\theta_V) = e^{-\tau/\mu_V} + t_d(\theta_V). \tag{35}$$

The third part is due to the reflectance of the atmosphere $\rho_a(\theta_S, \theta_V, \phi_{S-V})$, which is a function of the sun zenith angle, satellite view zenith angle and the difference between the sun azimuth and view azimuth angles.

For the TOA reflectance of a homogeneous Lambertian surface we get [2]

$$\rho_{TOA}(\theta_S, \theta_V, \phi_{S-V}) = \rho_a(\theta_S, \theta_V, \phi_{S-V}) + \frac{\rho_t}{1 - \rho_t S} T(\theta_S) T(\theta_V). \tag{36}$$

The gaseous absorption is taken into account by multiplying the right handside with the gaseous transmission T_g of the selected band. [2]

$$\rho_{TOA}(\theta_S, \theta_V, \phi_{S-V}) = T_g\{\rho_a(\theta_S, \theta_V, \phi_{S-V}) + \frac{\rho_t}{1 - \rho_t S} T(\theta_S) T(\theta_V)\}. \tag{37}$$

More about 6SV's absorption modelling can be found from Section 2.6.2. Equation (37) gives the TOA reflectance based on the surface reflectance. Initially 6SV was designed for this purpose, as the name refers, Second simulation of a satellite signal in the solar spectrum. However, 6SV can be used also for the simulation of the surface reflectance based on the satellite signal. This is made by solving the surface reflectance ρ_t from (37). For solving ρ_t a new variable is introduced [2]

$$\rho_t' = \frac{\rho_t}{1 - \rho_t S}. \tag{38}$$

It can be solved from (37).

$$\begin{aligned} \rho_{TOA}(\theta_S, \theta_V, \phi_{S-V}) &= T_g\{\rho_a(\theta_S, \theta_V, \phi_{S-V}) + \rho_t' T(\theta_S) T(\theta_V)\} \\ \rho_t' T(\theta_S) T(\theta_V) &= \frac{\rho_{TOA}}{T_g} - \rho_a(\theta_S, \theta_V, \phi_{S-V}) \\ \rho_t' &= \frac{\frac{\rho_{TOA}}{T_g} - \rho_a(\theta_S, \theta_V, \phi_{S-V})}{T(\theta_S) T(\theta_V)} \end{aligned} \tag{39}$$

From (38) we get the surface reflectance ρ_t.

$$\begin{aligned} \rho_t' &= \frac{1}{\frac{1}{\rho_t} - S} \\ 1 &= \rho_t'(\frac{1}{\rho_t} - S) \\ 1 + \rho_t' S &= \frac{\rho_t'}{\rho_t} \\ \rho_t &= \frac{\rho_t'}{1 + \rho_t' S} \end{aligned} \tag{40}$$

2.6.2 Absorption modelling

6SV's gaseous absorption model is based on HITRAN database. High-resolution transmission molecular absorption database, HITRAN, is a project started by the

US Air Force Cambridge Research Laboratories in the late 1960's. HITRAN'2004 contains information on 1,734,469 spectral lines for 37 molecules from the ultraviolet range to the microwaves [41]. 6SV models 6 molecules in the atmosphere. These are:

- Oxygen O_2
- Ozone O_3
- Water vapor H_2O
- Carbon dioxide CO_2
- Methane CH_4
- Nitrous oxide N_2O

The first four are the most important for the solar radiation [10]. 6SV assumes O_2, CO_2, CH_4 and N_2O to be constant and uniformly mixed in the atmosphere. H_2O and O_3 concentrations vary according to the location and time, which makes their modelling very important for a good radiative transfer modelling. 6SV divides the solar spectrum into 10 cm^{-}1 intervals by using HITRAN database. For each molecule, 6SV has a transmission band model. For water vapor, 6SV uses random exponential band model by Goody [42]. For other gases, random exponential band model by Malkumus is used [43]. When there are several absorbing gases, the total transmission is the product of each gas transmission. When the scattering and absorbing effects happen at the same time, the situation is a bit more complicated than described in 2.6.1 and above. The gaseous absorption have to be computed for every scattering path. [2]

2.6.3 Input and output files

6SV is used with input and output files. The input file is an ASCII file with specified lines for different parameters. When 6SV is run with the input file, 6SV makes the ASCII output file. For the atmospheric correction, a user has to set geometrical conditions, the type of atmospheric conditions, an aerosol model type, a target altitude, the altitude of airborne measurement, spectral conditions, a ground reflectance type and a TOA radiance or a reflectance. [2]

The type of atmospheric conditions is used for the selection of a pressure, temperature, water vapor and ozone profiles. The atmospheric condition types vary with latitude and season, or US62 standard atmosphere can be chosen. If the amount of ozone and the total precipitable amount of water vapor in atmospheric column is fed, US62's atmospheric profiles are scaled according to them. It is also possible to feed own atmosphere model, which includes pressure, temperature, water vapor and ozone profiles.[2]

The aerosol model types include, continental, maritime, urban, desert and biomass burning. In 6SV, there are ready made atmospheric conditions for the most common optical remote sensing instruments. These include Meteosat, GOES, AVHRR, TM, MODIS, POLDER, SEAWIFS, AATSR, MERIS and GLI. The target surface can be chosen to be heterogeneous or homogeneous. A heterogeneous surface means that the target surface type is different than the surface type around it. For example the target can be chosen to be lake water and environment around it can be chosen to be green vegetation. [2]

Example of an input file.

```
0               (User defined spectral conditions)
0 0 20 180 8 7  (sun zen; sun azi; view zen; view azi; month; day)
8               (Option for water vapor and ozone)
2 0.250         (water vapor; ozone)
1               (Continental aerosol model)
0               (AOD chosen)
0.5             (aod)
-0.3            (target altitude, negative value)
-1000           (sensor altitude)
74              (Chosen band)
0               (Homogeneous surface)
0               (No directional effects)
4               (Mean spectral value)
0               (Atm. correction Lambertian)
100             (radiance, positive value)
```

The 6SV is run with the following command.

```
sixsV1.0B <inputfile.INP> outputfile.OUT
```

The output file has several sections for the atmospheric conditions calculated by 6SV. At the end of the output file is a section for the atmospheric correction. The atmospheric correction section below was made by 6SV with the input file above.

```
*************************************************************
*                  atmospheric correction result            *
*                  -----------------------------            *
* input apparent reflectance           :    0.186           *
* measured radiance [w/m2/sr/mic]      :  100.000           *
* atmospherically corrected reflectance                     *
* Lambertian case :      0.06351                            *
* BRDF       case :      0.06351                            *
* coefficients xa xb xc                :  0.00344  0.27903  0.25111*
* y=xa*(measured radiance)-xb;  acr=y/(1.+xc*y)             *
*************************************************************
```

As mentioned above, the TOA value can be given as reflectance or as radiance. Depending on which is given, the other is calculated by 6SV. Here, the TOA radiance was given and the TOA reflectance was calculated. In the atmospheric correction results the surface reflectance and the atmospheric correction parameters, x_a, x_b and x_c are given. The surface reflectance is calculated with the following two equations.

$$\rho'_t = x_a L_{toa} - x_b \tag{41}$$

$$\rho_t = \frac{\rho'_t}{1 + x_c \rho'_t} \tag{42}$$

These correspond Equations (39) and (40) which were shown before. The atmospheric parameters are independent of the input reflectance/radiance, so they can be used with different input values. [2]

2.7 The atmospheric correction of MERIS Lakes processors

A Neural network has been used for an atmospheric correction in MERIS Lakes processors. The processors were mainly developed by Roland Doerffer from GKSS Research Center and they are part of BEAM VISAT 4.2 software. There are processors for Case-2 type coastal waters, boreal lakes and eutrophic lakes. The processors are Case-2 Regional processor, Boreal Lake processor and Eutrophic Lake processor. All processors are divided into two parts. The first part is a neural network for the atmospheric correction of MERIS data over water areas, which is same for all processors, except that the data used for the training of the neural network is modified to correspond the atmosphere of the region. The second part, MERIS Lake Water Algorithm, is a neural network for the estimation of water substances based on the atmospherically corrected MERIS data. It is trained according to the water type. In the thesis the atmospheric correction code using 6SV radiative transfer model is compared to the atmospheric correction of MERIS Lakes processors. Also MERIS Lake Water Algorithm is used with the 6SV atmospherically corrected radiance reflectance and with the radiance reflectance of the atmospheric correction of MERIS Lake processors. The estimates are compared to validation data. In the following the atmospheric correction algorithm of MERIS Lakes processors is described and in Section 2.9 MERIS Lake Water Algorithm is described. [44]

The atmospheric correction algorithm of MERIS Lakes processors calculates a water leaving radiance reflectance. It is defined in [44] to be the ratio of water leaving radiance $L_u(\theta_S, \theta_V, \phi_S, \phi_V)$ to downwelling irradiance E_d just above water surface. The algorithm takes into account the effects of air molecules, aerosols and thin clouds. It also takes into account the effects of foam and sun glint over water. The core of the algorithm is a neural network trained with photon trace Monte Carlo simulation data. The atmospheric correction procedure is described in more detail in Figure 8. Inputs (elements 1-4 in the figure) are given pixel by pixel, except for solar flux at TOA, which is same for all pixels. The input radiances consists of Channels from 1 to 10 and Channels 12 and 13. The surface pressure and the total column ozone are taken from the MERIS Level 1 product. [44]

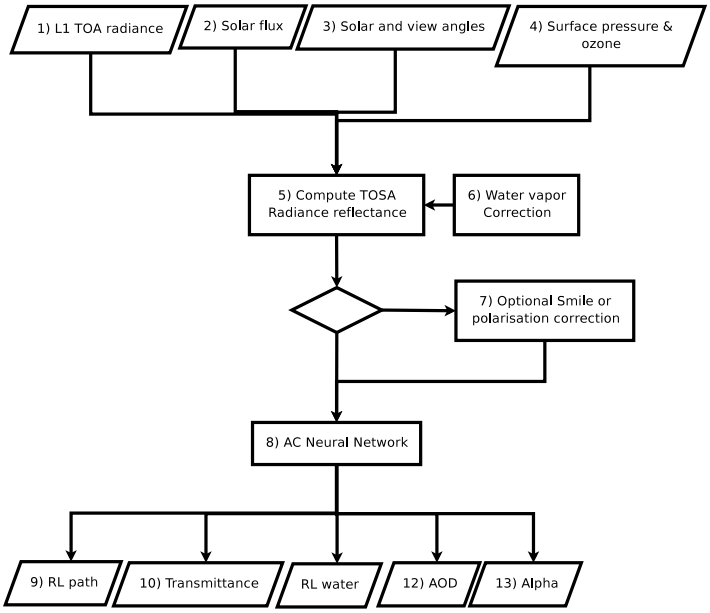

Figure 8: Flowchart of the atmospheric correction of MERIS Lakes processors. [44]

To reduce the number of variables, standard values for total column ozone, surface pressure and lake altitude are used. Their variations from the standard values are taken into account before the usage of the neural network in the element 5. Element 5 computes so called top of the standard atmosphere radiance reflectance, TOSA radiance reflectance, with standard Rayleigh scattering and ozone profiles. In the element 6, the effect of water vapor on Channel 9 is taken into account. In the element 7, there are optional correction procedures for the correction of a camera boundary problem and for the electromagnetic wave's polarization in the atmosphere. [44]

The element 8 is the neural network. It takes into account scattering and absorption from aerosols, thin cirrus clouds, sun and sky glint. It has been trained with data produced by a photon tracing Monte Carlo radiative transfer code. In the Monte Carlo code, the atmosphere is divided into 50 layers each 1 km deep. In one Monte Carlo run, atmosphere's optical parameters and water concentrations are randomly taken. Then a large number of photons is sent from the TOA to the atmosphere. For each photon, the distance between the collision events, the scattering angle and the water wave slope angle are randomly taken. The downward radiance is calculated from the number of photons arriving to the water surface. The reflection from the water is simulated with another neural network trained with data from Hydrolight model. The atmosphere's upward transmittance is calculated with the downward transmittance and an empirical correction coefficient. The data from Monte Carlo simulations relate the TOSA radiance reflectance at 12 MERIS channels and the view geometry to the water leaving radiance reflectance, the path radiance reflectance, the atmosphere's transmittances, AOD and Ångström coefficient. These data are used for the training of the neural network with a backpropagation error-

minimization method. About 66% of the simulation data is used for the training while 33% is kept as a test set to avoid overtraining. The neural network has 4 hidden layer (25x30x35x40) with fully connected neurons. For different regions of Europe, different training data have been used in the training, but the structure of the neural network is kept the same. The output of the neural network is also the output of the atmospheric correction procedure. [44]

2.8 Remote sensing of water quality

The quality of surface water is affected by the type and quantity of various suspended and dissolved substances. Optical water leaving radiance reflectance just above the water surface is affected by some of these substances. Optically, the most significant substances are chlorophyll-a, total suspended matter and colored dissolved organic matter. [5]

Chlorophyll-a is a pigment found in all phytoplankton. Phytoplankton is the base of aquatic food chain and its amount determines the productivity of the water. Chlorophyll-a has absorption lines at wavelengths of 430 nm and 665 nm, which causes the green color of phytoplankton. The concentration of chlorophyll-a, mas per unit volume [μg/l], characterizes the amount of phytoplankton in the water. The amount of chlorophyll-a can be estimated from satellites. [5]

Total suspended matter or total suspended solids affects on the optical properties of water. The total suspended solids are defined in [45] as the solids, which pass filter of 2 μm pore size. (However, some times filter with pore size of 0.45 μm is used in the definition). Solids include both in-organic and organic supended particles. The optical properties of in-organic suspended solids depend on the geological material of the region under investigation. The concentration of total suspended solids [mg/l] decreases when the distance from the shore line increases. Because of this, total suspended solids have a small effect on the optical properties of the oceans. [5] [45]

Gelbstoff (also known as colored dissolved organic matter, yellow substances, humus, gilvin and humic matter) consists of compounds produced during the decay of organic matter from forests, swamps, algae and phytoplankton. The absorption spectrum of gelbstoff is an exponential function with high absorption values at shorter wavelengths and small absorption after 700 nm. The scattering properties of gelbstoff can be ignored in remote sensing, because it is assumed that gelbstoff is fully dissolved. The amount of gelbstoff is characterized by the absorption coefficient at certain wavelength. Instead of measuring the amount of gelbstoff with the help of concentration, absorption coefficient is often used. [5]

These three optically significant substances and the water itself defines the inherent optical properties of lakes and the oceans. Optical properties of water can be divided to absorption, scattering and backscattering. Absorption is measured with absoption coefficient $a(\lambda)$, which is defined in [45] to be the fraction of the incident intensity I_0 which is absorbed per depth of the layer l passed by the radiation. The intensity

of the absorbed radiation is [45]

$$I_a(\lambda) = a(\lambda)\ l\ I_0(\lambda). \tag{43}$$

Scattering coefficient $b(\lambda)$ is defined in the same reference as the fraction of the incident intensity, which is scattered per depth of the scattering layer. The intensity of the scattered radiation is [45]

$$I_s(\lambda) = b(\lambda)\ l\ I_0(\lambda). \tag{44}$$

Backscattering coefficient $b_b(\lambda)$ is calculated in the same manner for the radiation, which is scattered in an angle of 90 degrees or greater. The angle is measured with respect to the incident direction of the propagation.[45]

$$I_b(\lambda) = b_b(\lambda)\ l\ I_0(\lambda). \tag{45}$$

The water leaving radiance reflectance is often connected to water's backscattering coefficient $b_b(\lambda)$ and absorption coefficient $a(\lambda)$ with equation by Kirk [46].

$$\rho_{RS}(\lambda) = 0.083\frac{b_b(\lambda)}{a(\lambda) + b_b(\lambda)} \tag{46}$$

For Finnish lakes, Kallio determined a relationship between the amount of chlorophyll-a concentration C_{Chl-a} and the absorption coefficient of phytoplankton pigments $a_{pig}\,(\lambda = 443nm)$. [47]

$$C_{Chl-a} = 62.6 * a_{pig}\,(\lambda = 443nm)^{1.29}\,[\mathrm{mg/m^3}] \tag{47}$$

He also developed an equation for the concentration of total suspended matter in Finnish lakes derived from scattering coefficient of water. [48] [49]

$$C_{TSM} = 1.042 * b\,(\lambda = 443)\,[\mathrm{g/m^3}] \tag{48}$$

Often water bodies are divided into two classes according to the significance of phytoplankton to the optical properties. Case-1 waters are defined to be waters in which the phytoplankton dominates the optical properties. This kind of water can be found from mid-oceans, where the amount of suspended matter and gelbstoff are small. Waters where phytoplankton is not dominating the optical properties are called Case-2 waters. These waters include inland waters, lakes and rivers. All Finnish lakes can be classified to Case-2. [5]

Secchi depth and turbidity are two other often used water parameters. The Secchi depth [m] characterize the transparency of the water. All substances affecting on the optical properties of water affect on the Secchi depth. It can be measured from a boat or shore by lowering standard size (diameter 12 to 20 cm) black and white disk to water. Secchi depth is the depth when the disk cannot be seen anymore by human eye. The measurement is always affected by lighting conditions and the vision of the observer. Empirical methods have been developed to derive Secchi depth from satellite data. Some of them are mentioned in [45]. The turbidity measures the optical scattering in water. There is not any standard method to measure turbidity on Earth's surface. However, turbidity measurements correlate with some satellite instrument's radiance measurements. This makes it possible to estimate turbidity from satellite data [45]

2.9 MERIS Lake Water Algorithm

MERIS Lake Water Algorithm is based on two neural networks, inverse model neural network and forward model neural network. The inverse neural network relates water leaving radiance reflectances at eight MERIS channels and view geometry to inherent optical properties of water at 443 nm, absorption coefficient of phytoplankton a_{pig}, scattering coefficient of total suspended matter b_{tsm} and absorption coefficient of dissolved organic matter a_{gelb}. The forward neural network relates optical properties of water to the water leaving radiance reflectances. The inverse model is used to get an initial guess for the iterative use of forward model. First the atmospheric corrected radiance reflectances are fed to the inverse model. The output of the inverse model is set as an input to the iterative process, which uses Levenberg-Marquardt minimization algorithm. The iteration is stopped when the relative error change is less than 3 % or when 10 iterations have been reached. The algorithm gives also a parameter indicating the quality of the estimation. The concentration of total suspended matter dry weight and phytoplankton chlorophyll are calculated from the inherent optical properties of water with simple relations. [51]

Both neural networks were trained with simulated data. The data were simulated with Hydrolight radiative transfer code, which is based on a bio-optical model developed with in situ measurements from Finnish and Spanish lakes. Hydrolight code was used to produce over 60 000 samples relating the water leaving radiance reflectance and view geometry to the inherent optical properties of water, total suspended matter concentration and chlorophyll concentration. Models for lakes in different parts of Europe were used with different in situ and simulation data. Algorithms for Finnish boreal lakes and for Spanish eutrophic lakes were developed. Before the MERIS Lakes project, an algorithm generally for Case-2 type of waters was developed. [51]

3 Instruments and data used in the thesis

The optical radiance measurements used in this thesis are provided by MERIS satellite instrument. For an accurate atmospheric correction, information on the atmosphere is needed. The parameters required by the 6SV radiative transfer code are aerosol optical depth, precipitable water vapor in the atmosphere column and total amount of ozone in atmosphere column. Measurements of aerosol optical depth and water vapor in the atmosphere are provided by NASA's MODIS satellite instrument. Ozone measurements are provided by NASA's OMI satellite instrument. In the thesis, AOD measurements from weather station are used for the scaling of the AOD satellite measurements. For the validation of the atmospheric correction code in situ measurements from Finnish lakes are used. In this chapter, all data used in the thesis are described.

3.1 MERIS satellite instrument

Medium Resolution Imaging Spectrometer Instrument (MERIS) is carried by ESA's Envisat earth observation satellite. The main aims of the Envisat mission are to provide continuity of earlier remote sensing missions, to enhance especially ocean and ice remote sensing missions, to extend the range of observable environmental parameters and to make a significant contribution to environmental studies, especially to atmospheric chemistry and ocean studies [52]. Envisat was launched on March 2002 and originally it was planned to work for five years. However, ESA member states have agreed to fund the project until 2010 [53]. Envisat has a sun-synchronous near-polar orbit with 800 km mean altitude. The satellite is in its orbit's descending node at 10:00 a.m. UTC time. One orbit takes 101 minutes and the repeat cycle of the orbit is 35 days [54]. Besides MERIS, Envisat has nine other instruments. These include Advanced Synthetic Aperture Radar (ASAR), Advanced Along Track Scanning Radiometer (AATSR), and GOMOS.

The primary mission of MERIS is to measure the sea color in the oceans and coastal areas. The knowledge of sea color can be converted to the measurements of chlorophyll pigment concentration, suspended sediment concentration and atmospheric aerosol loads over water. MERIS measures solar radiation reflected by the Earth with fifteen channels on visible and near-infrared spectral region. Each channel has a programmable width and location between 390 nm and 1040 nm. However, usually fixed widths and locations are used. The fixed channels and their primary use is presented in Table 2. MERIS uses a push-broom technique. The across-track sampling is performed electronically and the along-track sampling is performed with the help of satellite's motion.

MERIS provides global coverage within two to three days. It provides data with three spatial resolutions. Full resolution (300 m x 300 m at nadir), reduced resolution (1.2 km x 1.2 km at nadir) and low resolution (4.16 km x 4.16 km at nadir). The instrument takes an image with the full resolution. Reduced resolution and low

Table 2: The fixed set of MERIS bands and their applications. [3]

No.	**Band center** [nm]	**Band width** [nm]	**Applications**
1	412.5	10	Yellow substance and detrial pigments
2	442.5	10	Chlorophyll absorption maximum
3	490	10	Chlorophyll and other pigments
4	510	10	Suspended sediments, red tides
5	560	10	Chlorophyll absorption minimum
6	620	10	Suspended sediments
7	665	10	Chlorophyll absorption and fluorescence reference
8	681.25	7.5	Chlorophyll fluorescence peak
9	708.75	10	Fluorescence reference and atmospheric corrections
10	753.75	7.5	Vegetation, cloud and O_2 absorption band reference
11	760.625	3.75	O_2 R branch absorption band
12	778.75	15	Atmospheric corrections
13	865	20	Atmospheric corrections
14	885	10	Vegetation and water vapor reference
15	900	10	Water vapor

resolution images are averaged from the full resolution image. The full resolution products are delivered in scenes of 575 km x 575 km or 296 km x 296 km. Reduced resolution products are delivered in the scenes of 1150 km x 1150 km. The MERIS products are also provided with three processing levels. Level 1 products present the top of the atmosphere radiance. Level 2 products are produced from the Level 1 products and they present geophysical properties, e.g. total water vapor content in an atmospheric column and surface radiance over ocean. Level 3 products are constructed from more than one MERIS product to display average geophysical measurements over a time period. [3] In this thesis, Level 1 full resolution products are used. Besides the radiance data, MERIS Level 1 full resolution data include other data presented at selected tie points of the product. The tie point data consist of

- latitudes and longitudes
- altitude of the surface from the sea level derived from DEM
- roughness of the surface derived from digital roughness model
- DEM latitude and longitude corrections
- sun zenith angles, sun azimuth angles, view zenith angles, view azimuth angles

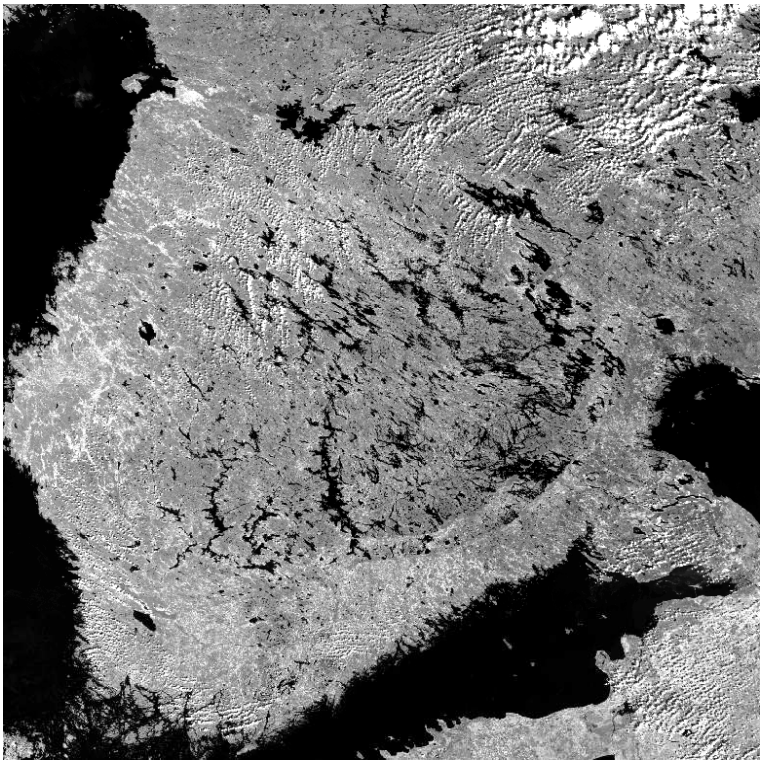

Figure 9: An example of MERIS Level 1 radiance data set used in the thesis. MERIS Channel 10 on 7th of August 2007.

- zonal and meridional wind from ECMWF
- sea level pressures from ECMWF
- total ozone from ECMWF
- relative humidity from ECMWF

MERIS full resolution data product is very suitable for water quality measurements because of its narrow field of view. The narrow field of view is especially needed for Finnish lakes, which many times are quite small and have complex shape [5]. In Figure 9, an example of the data set used in this thesis is presented. It presents radiance on MERIS Channel 10 over southern Finland captured on 7th of August 2007.

3.2 MODIS satellite instrument

MODIS (Moderate Resolution Imaging Spectroradiometer) instruments are carried by two NASA's EOS satellites, Terra (EOS AM) and Aqua (EOS PM). Both satellites have orbits at 705 km altitude. Both have a sun-synchronous near-polar circular orbit. Terra is at the descending node of its orbit at 10:30 a.m. and Aqua at 1:30

p.m.. These satellites provide global coverage for MODIS data in one or two days. [56]

MODIS measures radiance at wavelengths from 0.405 μm to 14.5 μm with 36 channels. The spatial resolution at nadir varies so that two channels have resolution of 250 m x 250 m, five channels have a resolution of 500 m x 500 m and remaining 29 channels have resolution of 1 km x 1 km. The width of a MODIS's scene is 2330 km. For scanning, MODIS uses a rotating double-sided mirror. NASA provides atmospheric data products derived from the MODIS measurements without charge. The data are not copyrighted, although NASA requires that the source of the data is mentioned in the research publications. The following sentence have to be included to all publications which use MODIS data, as it is done here.

Data used in this research include data produced through the funding of NASA's Earth Science Enterprise (ESE) Earth Observing System (EOS) program.

In this thesis MODIS aerosol and MODIS water vapor data products are used as atmospheric data for the 6SV atmospheric correction. As well as the atmospheric data, both data products include also a latitude, longitude, time, solar angles, viewing angels and quality control data. The products are delivered in the HDF4 format developed and supported by the National Center for Supercomputing Applications. The filename starts with "MOD" if the data set is from Terra satellite and with "MYD" if the data set is from Aqua satellite. The date of the satellite capture is given in the filename as a Julian date. [56]

3.2.1 MODIS aerosol product

MODIS aerosol data product monitors AOD over the oceans globally and over a portion of the continents. The spatial resolution of the product is 10 km x 10 km at nadir. As well as AOD data there are other aerosol data. MODIS aerosol product provides classification of aerosol type over land. The types are mixed, dust, sulfate, smoke and heavy absorbing smoke. Over the oceans, aerosol distribution is calculated. There are also Ångström exponent data derived from measurements at 0.47 μm and 0.67 μm. In this thesis, the data set called *Optical_Depth_Land_And_Ocean* of the MODIS aerosol product is used. This data set contains AOD over land and ocean at 0.550 μm. In Figure 10, is the data set used for the atmospheric correction of the MERIS data set presented in Figure 9. As can be seen from the figure the data set is spatially sparse. AOD is not given at all points of the image. This is typical for the MODIS aerosol product.

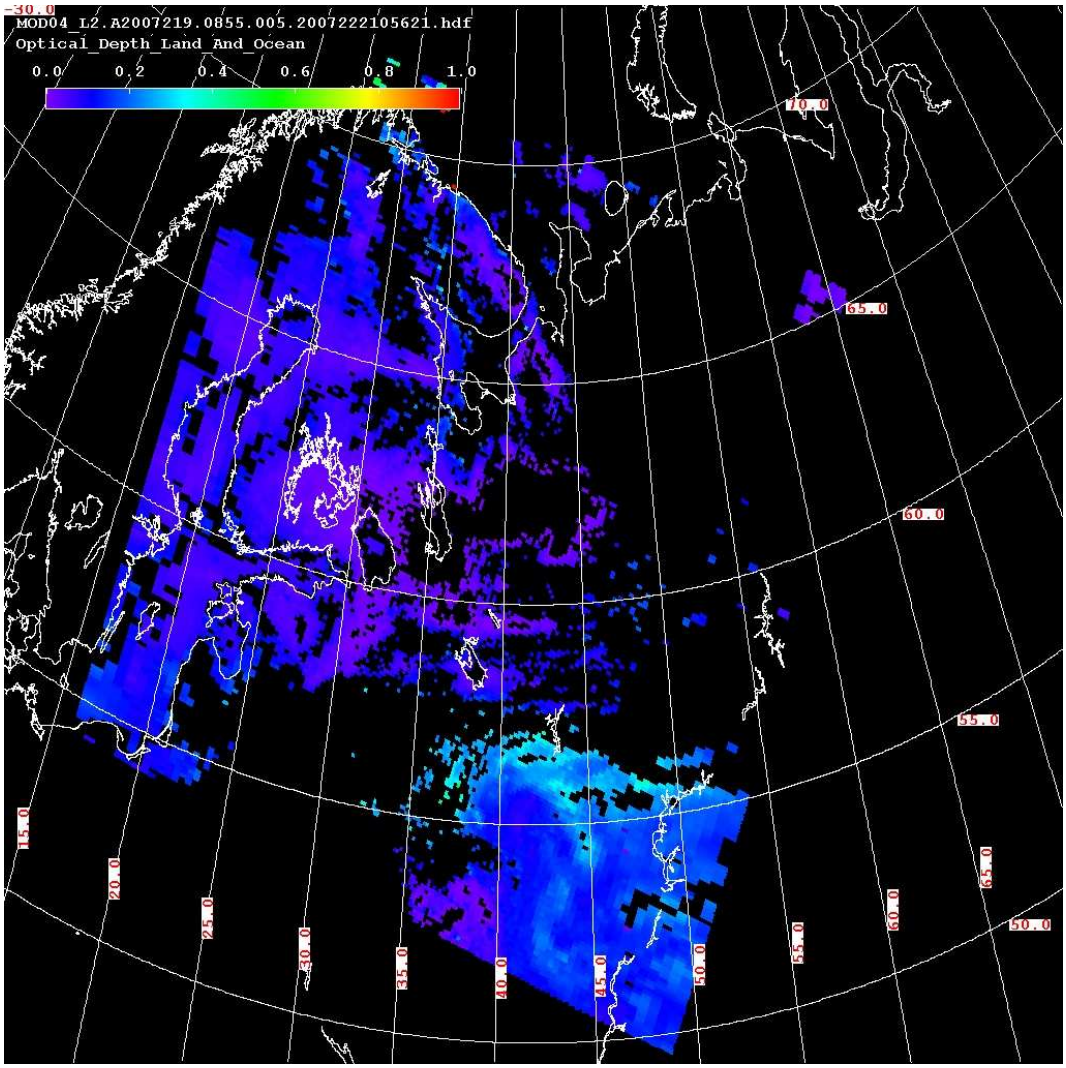

Figure 10: Data set *Optical_Depth_Land_And_Ocean* from the MODIS aerosol product of 7th of August 2007. The data set presents aerosol optical depth over North Europe. Source of the figure *http://ladsweb.nascom.nasa.gov*.

3.2.2 MODIS precipitable water vapor product

MODIS precipitable water vapor product gives the amount of water vapor in an atmosphere column in cm. In the product, the water vapor content is calculated with two algorithms, one from a near-infrared channel and another from an infrared channel. The data are delivered in the spatial resolution of 5 km x 5 km. In this thesis, the data set, *Water_Vapor_Near_Infrared*, is used. In Figure 11 is the data set used with the 6SV radiative transfer code to the atmospheric correction of Figure 9.

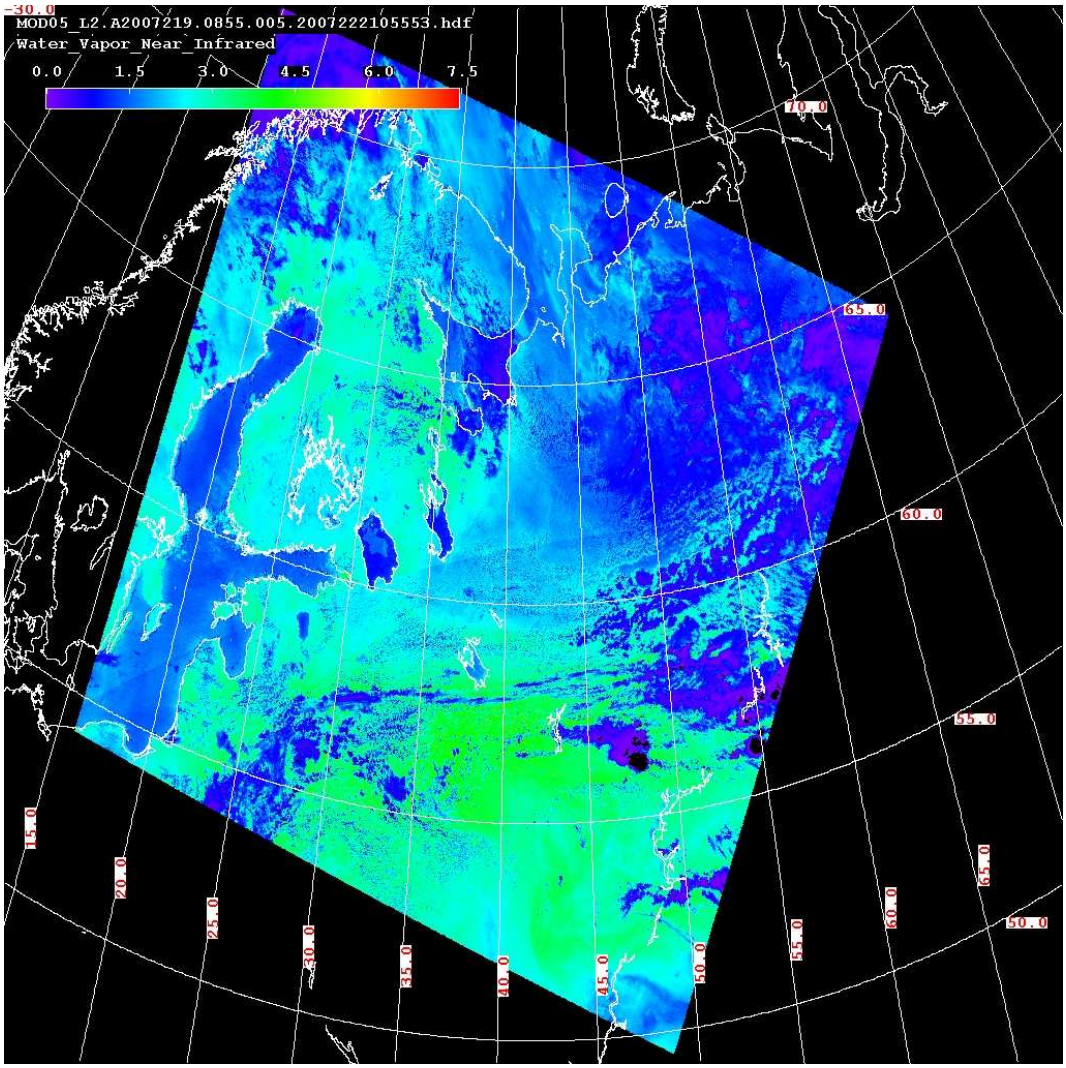

Figure 11: Data set *Water_Vapor_Near_Infrared* from the MODIS water vapor product. Data presents precipitable water vapor over Northern Europe on 7th of August 2007 in cm. Source of the figure *http://ladsweb.nascom.nasa.gov*.

3.3 OMI satellite instrument and ozone product

Ozone Monitoring Instrument (OMI) is carried by NASA's Aura satellite, part of NASA's EOS program. OMI is developed by Netherlands's Agency for Aerospace Programs (NIVR) in collaboration with the FMI. Aura was launched on 2006 and it is designed to work for six years. Aura has a near-polar, sun-synchronous orbit at altitude of 705 km. It has a period of approximately 100 minutes and it flies 15 minutes behind the Aqua satellite.

OMI has two spectrometers using CCD detectors.Their spectral ranges are at visible part of the spectrum at 350 - 500 nm, and at ultra-violet range at 270 - 314 nm and 306 - 380 nm. The spectral resolution is 0.45 - 1 nm. The instrument has a 2600 km wide swath. This wide swath makes possible to have daily global observations. OMI data are delivered with pixel size of 13 km x 24 km at nadir. The OMI data products include interesting data products in the context of the thesis. These are aerosol extinction, AOD, aerosol single scattering albedo, total column ozone, ozone profiles, ozone tropospheric column and Lambert Equivalent Spectral Surface Reflectance. OMI data products have also measurements of clouds, atmosphere's content of nitrogen and sulphur dioxide. However, only the OMTO3 total column ozone product was used in the thesis. It contains estimates of the amount of ozone in an atmosphere column measured in Dobson units. OMTO3 data product's algorithm is based on the algorithm of TOMS instrument. [57] [58]

3.4 Weather station AOD data

In the thesis satellite measurements of AOD are used together with in situ measurements of AOD. The in situ measurements are made at Jokioinen at FMI's weather station. The weather station measures AOD daily with a sunphotometer at wavelengths of 368.5 nm, 411.9 nm, 499.6 nm and 862.1 nm. However, in the thesis, AOD measurement at 550 nm were needed. They were derived from Ångström law presented in Equation (24). Empirical coefficient of Ångström law, α and β, were calculated with the help of linear regression and the AOD measurements of Jokioinen. The satellite AOD data are scaled with the in situ measurement $\tau_{A,insitu}$ to increase the quality of the estimate. The scaled values are given by

$$\tau_{A,s} = \frac{\tau_{A,insitu}}{\tau_A(i,j)} \cdot \tau_A, \tag{49}$$

where τ_A is the initial satellite measurement to be scaled and $\tau_A(i,j)$ is the satellite data set's value at location of in situ measurement. AOD values used in the thesis are shown in Table 3.

3.5 Validation data

Water leaving radiance reflectances were measured on Finnish lakes during the summer of 2007. The measurements were made at three locations: at Lake Pyhäjärvi

Table 3: AOD at 550 nm from Jokioinen's weather station (latitude: 60^o 48' 49.9", longitude: 23^o 30' 03.3") used for the scaling of satellite data.

Date (2007)	Time (UTC)	$\tau_{A,insitu}(550nm)$
June 1	9:23	0.0648
June 2	8:50	0.0765
June 3	9:57	0.0729
June 4	9:19	0.0804
June 5	8:54	0.112
June 7	9:34	0.0963
June 8	8:57	0.0474
August 8	-	0.0690
August 23	-	0.0699

at Säkylä, Lake Päijänne and Lake Vesijärvi. The times and the locations of the measurements are in Table 4. Lake Pyhäjärvi's measurements were part of Catch Lake program, funded by TEKES Finnish Funding Agency for Technology and Innovation, and carried out by Helsinki University of Technology and Finnish Environmental Institute. The measurements at Lake Päijänne and Lake Vesijärvi were part of MERIS Lake program, funded by ESA and carried out by Helsinki University of Technology and Finnish Environmental Institute.The water leaving radiance reflectance measurements were made with ASD FieldSpec FR Jr spectrometer. The most important parameters of the equipment are presented in Table 5. The radiance reflectances were measured on the spectral range from 399 nm to 949 nm with a spectral resolution of 1 nm. These reflectances were averaged for the spectral resolution of MERIS bands. In Figure 12 the water leaving radiance reflectances measured at three sites on 7th of August 2007 are shown. In all sites turbidity, Secchi depth, and concentrations of chlorophyll-a and total suspended matter were also measured. In Table 6 values of the measurement are shown on all days. In Table 7 the times of the satellite data and the in situ measurements of AOD can be compared to the times of the validation data in Table 4.

Table 4: The times and locations of the in situ measurements.

Site	Date (2007)	Time (UTC)	latitude [decimal degrees, WGS84]	longitude [decimal degrees, WGS84]
1	June 4	8:21	61.00933	25.61783
2	June 4	10:10	61.14283	25.48100
3	June 4	11:30	61.23033	25.54317
1	August 7	8:10	61.00933	25.61283
2	August 7	9:21	61.14150	25.47700
3	August 7	10:53	61.23133	25.54750
1	August 23	8:05	61.04855	22.22450
2	August 23	8:40	61.01203	22.27923
3	August 23	9:15	60.94010	22.34600

Table 5: The product specifications of ASD FieldSpec FR Jr.[59]

FieldSpec FR Jr	
Spectral range	350 nm - 2500 nm
Spectral resolution	3 nm @ 700 nm 30 nm @ 1400/2100 nm
Sampling Interval	1.4 nm @ 350 - 1050 nm 2 nm @ 1000 - 2500 nm
Scanning time	100 ms

Table 6: The in situ water quality measurements used in the thesis.

Site	Date (2007)	C_{Chl-a} [mg/l]	C_{TSM} [mg/l]	Turbidity [FNU]	Secchi depth [m]
1	June 4	0.94	2.6	3	2.9
2	June 4	0.73	2	2.3	3.7
3	June 4	1.50	0.8	0.86	5
1	August 7	0.60	2.2	1.9	2.9
2	August 7	0.49	1.2	1.1	4.6
3	August 7	1.37	0.7	0.62	4.9
1	August 23	0.88	2	1.7	3.5
2	August 23	0.82	2	1.5	3.6
3	August 23	0.82	2	2.3	3.6

Table 7: The times and dates of the MERIS, OMI, MODIS and the in situ AOD data used in the thesis. Time in UTC.

Date (2007)	MERIS	OMI	MODIS	AOD_{insitu}
June 1	9:20	7:56	10:15	9:23
June 2	8:41	7:00	9:05	8:50
June 3	9:57	6:03	10:05	9:57
June 4	9:27	21:38	8:55	9:19
June 5	8:55	9:10	9:50	8:54
June 7	9:32	8:58	9:40	9:34
June 8	9:01	8:02	10:10	8:57
August 7	9:15	15:00	8:55	-
August 23	9:12	8:23	10:35	-

4 Validation of the atmospheric correction code

4.1 The atmospheric correction code based on 6SV radiative transfer code

For an atmospheric correction using a radiative transfer code and atmospheric data, a MATLAB code was developed by the author. The basic idea is to take the atmospheric data from different satellite instruments, compute atmospheric correction parameters in a grid on the MERIS image to be corrected and interpolate the correction to all pixels. Two radiative transfer codes were tested for this project, MOSART and 6SV. The 6SV radiative transfer code was found to be more reliable and suitable for the project. It is also more tested and more documented in the literature.

The correction code consists of several parts. First a MERIS data set is read from a N1-file. For this `readproduct.m` MATLAB function is used. It is originally written by Ville Bergholm at the TKK's Laboratory of Space Technology in 2003. It is modified for the atmospheric correction code by the author. If the coordinates of the region of the interest (ROI) are given in map coordinates, they are converted to pixel coordinates of the image at this point. For the conversion, a function called `map2pixel.m` is used. It uses linear regression to find the dependency between the map coordinates and the pixel coordinates.

After this, the latitudes and longitudes are interpolated in ROI with function `interpolation_in_roi.m`. Later they are needed for the selection of the atmospheric data. Next the tie points are selected for the computation. Every second MERIS tie point is selected, starting from the upper left corner of the picture. Next, atmospheric satellite products are read with functions, `read_MOD04.m`, `read_MOD05.m` and `read_OMI.m`. `read_MOD04.m` reads AOD data from a MODIS aerosol product and `read_MOD05.m` reads precipitable water vapor data from MODIS data product. Both functions use MATLAB's built in functions for the reading of HDF4-data. `read_OMI.m` reads a OMI total column ozone product by calling H5dump software from the command line.

The selection of the AOD, water vapor and ozone values for every computation point is performed next. This is done with the help of `value_from_grid.m` function and the latitude and longitude grids. If constant value for the AOD, water vapor or for ozone is chosen, it is set there for every tie point inside ROI. After this, there is an option for the scaling of AOD satellite data with a in situ measurement according to Equation (49).

Next 6SV is run for the channels to be corrected and for every grid point. For every 6SV usage, a 6SV input file is written. From the output file solar constant and atmospheric correction parameters are read. After the use of 6SV, the atmospheric correction parameters are interpolated in all pixels of the ROI. Finally, the atmospherically corrected reflectances are calculated according to Equations (41) and (42). In Appendix A, the main function of the atmospheric correction code, `ACC.M`, and all functions called by it are described.

The atmospheric correction code was used with a computer corresponding to Pentium III NT 867. It took around four hours to make an atmospheric correction for a whole MERIS satellite image.

The performance of the implemented atmospheric correction code was tested in several ways with the help of validation data described in Section 3.5. First, atmospherically corrected MERIS data of 7th of August 2007 were compared to the in situ radiance reflectance of the same day. The atmospheric correction was performed with and without the AOD scaling. After that, the sensitivity of the correction for different input parameters was tested. Then the performance of atmospheric correction code was compared to the atmospheric correction of MERIS Lakes processors. It was also studied if the 6SV based atmospheric correction code or the atmospheric correction of MERIS lakes processors decrease the percentual variation in the satellite signal. The surface reflectances estimated with both corrections were used as the input of the MERIS Lake Water Algorithm and their results were compared. After that, it was studied if the 6SV atmospherically corrected data correlate better with the in situ data than the uncorrected data. Finally, the performance of the 6SV based atmospheric correction on land surface was studied.

The validation data and the output of atmospheric correction of MERIS Lakes processors have measurements of radiance reflectance. However, the 6SV gives an estimate of the reflectance (irradiance reflectance) of Lambertian surface according to Equation (8). Thus all 6SV reflectances were divided with pi to get the radiance reflectances.

4.2 Atmospheric corrections with and without AOD scaling

In Figure 12 TOA reflectance, the 6SV atmospherically corrected radiance reflectance and the in situ radiance reflectance measured on 7th of August 2007 are shown. The figure shows reflectances over lake water at three sites from Lake Päijänne area. Sites 1 and 2 are from Lake Vesijärvi and Site 3 is from Lake Päijänne. TOA reflectance has an exponential shape at all sites. This is caused by the scattering of the atmosphere, which is the stronger the shorter wavelength is.

The in situ radiance reflectance is significantly smaller than TOA reflectance. While the TOA reflectance is around from 1 % to 15 %, the in situ radiance reflectance is from 0.001% to 0.1%.

Between the TOA reflectance and the in situ radiance reflectance is the water leaving radiance reflectance estimated with 6SV radiative transfer code from the TOA radiance and atmospheric data. The atmospheric data included aerosol optical depth, total column ozone and precipitable water vapor in the atmosphere column. At Sites 1 and 2, the 6SV radiance reflectances have roughly the same shape as the in situ radiance reflectances. However, the values are much larger. The 6SV radiance reflectance varies from 0.4 % to 1 %. Also at Site 3, the 6SV radiance reflectance has different level than the in situ radiance reflectance, but also the shape of the

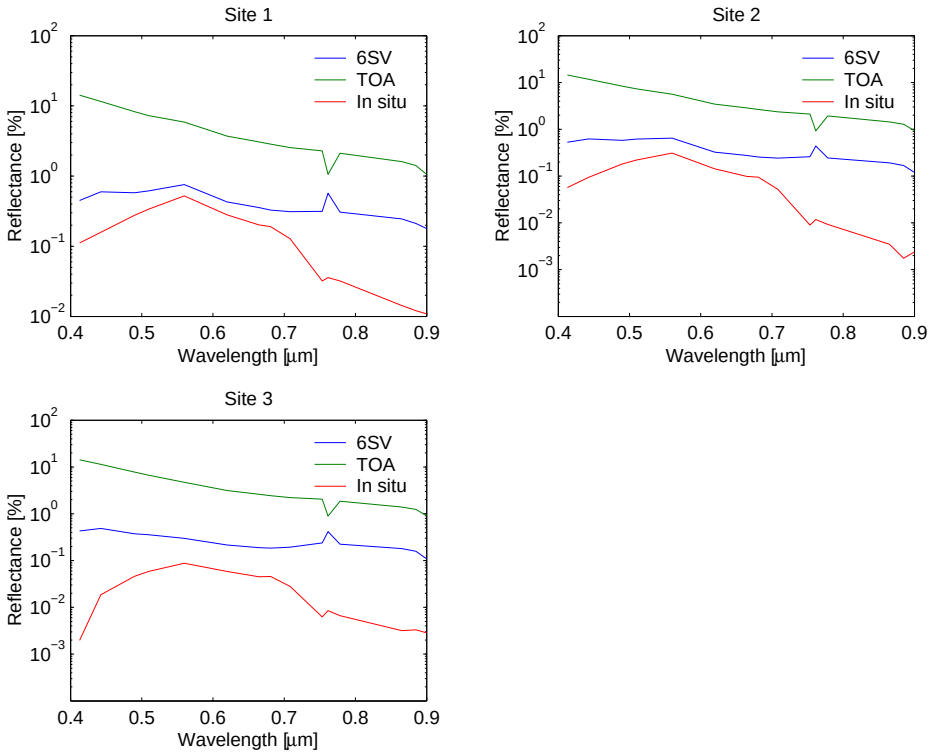

Figure 12: The surface radiance reflectances estimated with 6SV, TOA reflectances and in situ radiance reflectances on 7th of June 2007 at three sites at Lake Päijänne area.

curve is quite different from the in situ radiance reflectance. On Channel 11 (760.25 nm) a peak in the surface reflectance can be found. It is caused by the absorption line of the oxygen. It can be seen in the TOA reflectance and the in situ reflectance, as well. Channel 11 is usually used for the measurement of a cloud's altitude. At its spectral range it is relatively dark on the Earth's surface [61]. Channel 11 is problematic for the 6SV atmospheric correction. Instead of smoothing the oxygen absorption line, the atmospheric correction makes a peak there. 6SV is expecting that the water leaving radiance reflectance should have a peak at that wavelength to have the amount of radiation measured at the top of the atmosphere.

The absolute error between the 6SV estimated surface radiance reflectance and the in situ radiance reflectance is smallest on spectral range between Channels 4 and 8 (0.510 μm and 0.681 μm). On the same range also the in situ radiance reflectance has the largest values. This might indicate that the 6SV is not capable to simulate the radiative transfer when the surface radiance reflectance is too small. According to Behnert et al. in [60] the path radiance from the atmosphere can be more than 10 times larger than the radiance from water. This makes the atmospheric correction of water reflectance very sensitive to errors in the atmospheric correction.

An atmospheric correction was also made with AOD measurement from FMI's weather station in Jokioinen. The AOD values of MODIS data product were scaled

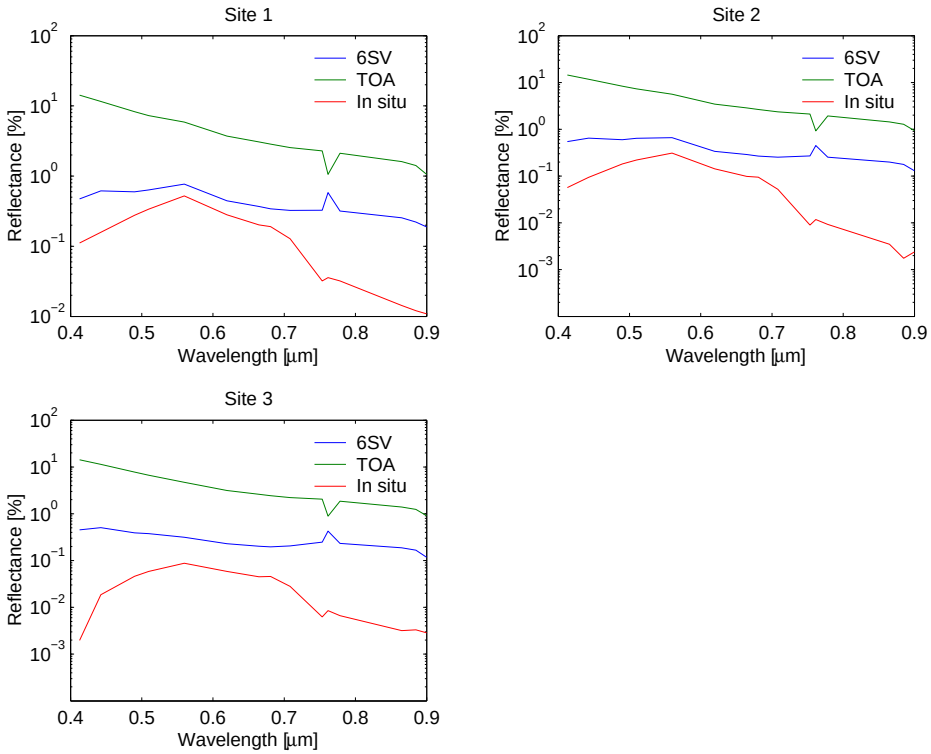

Figure 13: Water leaving radiance reflectance estimated with 6SV, TOA reflectance and in situ radiance reflectance on 7th of August 2007 at three sites at Päijänne area. In the figure is the same situation as in Figure 12, except that the AOD values were scaled using in situ measurement made at Jokioinen.

with the value measured at Jokioinen on the day of satellite overfly according to Equation (49). The 6SV radiance reflectance, the corresponding TOA reflectance and the in situ radiance reflectance are presented in Figure 13. The in situ AOD was smaller than the satellite measurement made over the weather station. The ratio of the in situ measurement to the satellite measurement is 0.8519. This decreases all AOD values used in the 6SV simulation. Smaller AOD means that less radiation is scattered to the sensor by the atmosphere and areas near the lake water. Because of this the surface radiance reflectance is estimated to be larger by 6SV. The difference between the radiance reflectance estimated with scaled AOD values and the radiance reflectance estimated with unscaled AOD values is small, as can be seen from Figure 14. However, the radiance reflectance estimated with scaled AOD values is always larger. Also the difference is greater at smaller wavelength, where the scattering effect is stronger.

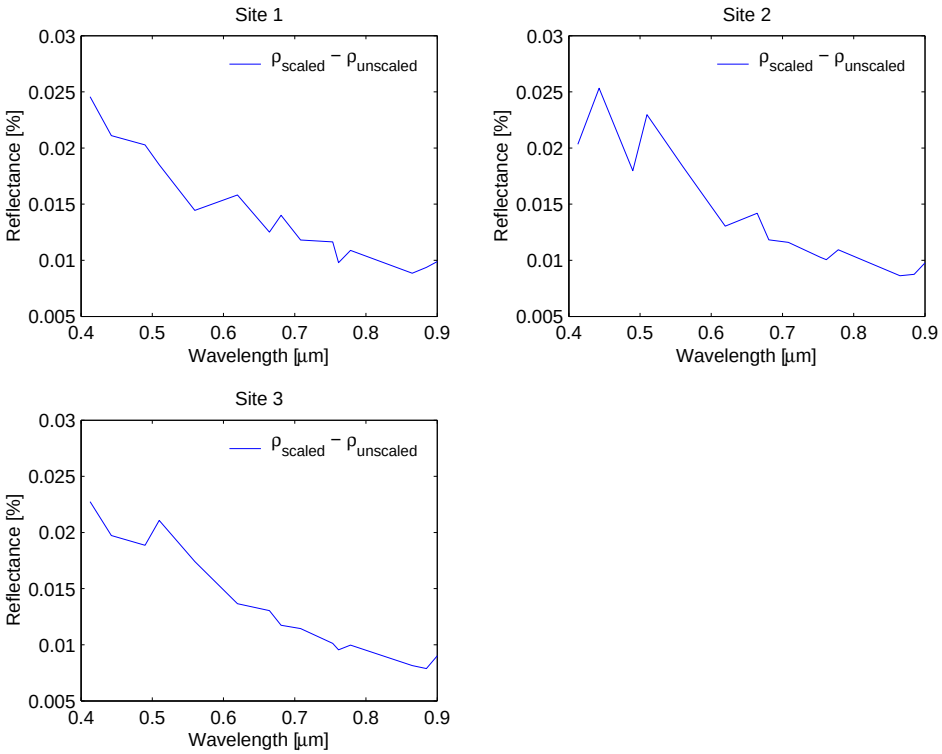

Figure 14: Difference between the water leaving radiance reflectances estimated with and without scaled AOD values.

4.3 Sensitivity of the atmospheric correction for the input parameters

The sensitivity of the atmospheric correction for input data was studied. The same MERIS data set as in Section 4.2 was corrected with different values of total column ozone, precipitable water vapor and AOD. One parameter was changed at the time while others were kept at the values of the satellite data. The atmospheric correction's sensitivity for total column ozone was tested with 284.5 DU and 330 DU. The total column ozone was noticed to have a relatively small effect on the correction of the wavelengths from 0.4 μm to 0.75 μm. The more ozone, the greater is the estimated surface radiance reflectance. At wavelengths longer than 0.75 μm, ozone had no effect at all.

The effect of precipitable water vapor was studied in the same way. For the same MERIS data product, an atmospheric correction with different water vapor values was made. The values from the MODIS water vapor product (around 2 cm) and constant values of 2 cm and 9 cm were used. Water vapor was noticed to have an effect on Channels 9 (0.709 μm) and 15 (0.900 μm). The more there is water vapor, the greater is the estimated surface radiance reflectance. On other MERIS channels, water vapor has no effect on the estimated radiance reflectance.

Neither the total column ozone nor the precipitable water vapor has an effect on

the over all shape or level of the surface radiance reflectance. They have only a small effect on certain wavelengths. This is different with the AOD. The effect of AOD was tested with similar manner. Eleven different values were tested. These were 0.0001, 0.0513, 0.1054, 0.1625, 0.2231, 0.2877, 0.3567, 0.4308, 0.5108, 0.5978 and 0.6931. These values were chosen because according to Equation (19) the first value corresponds to the transmittance value of 0.9999 and the rest correspond to transmittance values from 0.95 to 0.50 in 0.05 intervals. The corrections made with these AOD values at Site 1 are presented in Figure 15 together with the in situ radiance reflectance of Site 1. When AOD decreases, the estimated surface reflectance increases. This is the same effect which happened with the scaling of AOD satellite data with the in situ AOD measurement. Smaller AOD means that more light must be reflected from the target itself and not from the areas around it or from the atmosphere. From Figure 15, we can see that the AOD has a great effect on the level of the estimated surface reflectance. The larger the AOD is, the lower the surface reflectance is estimated. When AOD is 0.2231 or larger, the surface radiance reflectance is negative at some or all wavelengths. The AOD also has an effect on the shape of the curve. The larger the AOD, the more curved the estimated surface radiance reflectance. The AOD has more effect on shorter wavelengths than on longer wavelengths.

AOD seems to have a crucial effect on the modelling of scattering, because it affects on the whole MERIS spectrum and its effect is stronger at short wavelengths. Total column ozone and precipitable water vapor have a effect only on their absorption lines. This effect is small compared to the effect of AOD. According to the 6SV radiative transfer code, the scattering effect of atmosphere dominates the detected radiance reflectance of lake water measured at the top of the atmosphere. Also according to 6SV the scattering is mostly caused by aerosols.

One of the main reasons for the failure in the estimation of surface radiance reflectance in Section 4.2 might be that the AOD data are inaccurate. The aerosols vary greatly depending on the time and location [44]. According to Doerffer in [44] the optical properties of the atmosphere should be derived from the radiance measurement itself because of the rapid changes of aerosols. In this thesis the AOD data are from different satellite instrument. The AOD data are from MODIS aerosol product which has spatial resolution of 10 km. Also the difference in the capture time of AOD data and radiance data (20 min in the atmospheric correction of Section 4.2) may decrease the quality of the surface radiance reflectance estimate. The atmospheric correction parameters are computed in a grid of 60 km x 60 km. However, MERIS radiance data have a pixel size of 300 m x 300 m. Also this may decrease the accuracy of the estimated surface reflectance.

Also the 6SV's modelling of aerosols might not be accurate enough. The only aerosol data which were given to the 6SV in this thesis were AOD value and the aerosol model type (continental in all atmospheric corrections). From the aerosol model the spectral behavior of aerosols is derived. A better option would have been to give 6SV some information of the exponential behavior of aerosols at the moment of the satellite's overfly, for example Ångström exponent. However, according to Doerffer

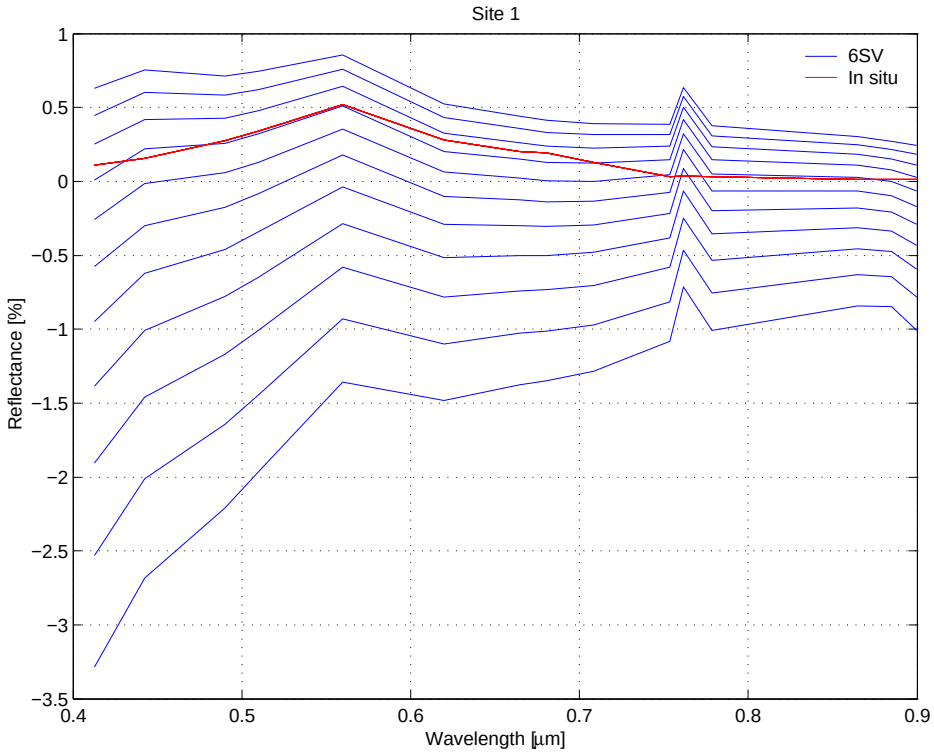

Figure 15: Surface radiance reflectance on 7th of August 2007 at Site 1 estimated with AOD values of 0.0001, 0.0513, 0.1054, 0.1625, 0.2231, 0.2877, 0.3567, 0.4308, 0.5108, 0.5978 and 0.6931. The highest radiance reflectance curve corresponds the smallest AOD, and the lowest curve corresponds the largest AOD. The AOD affects on the level and shape of the curve. When AOD is larger than 0.2231, the surface radiance reflectance is estimated to be negative at some or all wavelengths.

in [44] even this assumption does not work for the atmospheric correction of MERIS water measurement. A more sophisticated method is needed for the modelling of AOD's spectral behavior.

Another drawback of 6SV's aerosol modelling is that it is not modified to Finnish atmosphere. According to Behnert et al. in [60] "the Ångström wavelength exponents of the aerosol model used for atmospheric correction should be compared with measured data of the site under consideration." This is not done for the 6SV's aerosol model.

4.4 The atmospheric correction of MERIS Lakes processors

An atmospheric correction was also made with Case-2 Regional (C2R) processor for the same satellite data set of 7th of August 2007. As described in Section 2.7, Case-2 Regional processor has the same atmospheric correction algorithm as other MERIS Lakes processors. It estimates surface radiance reflectance at MERIS Channels from 1 to 10 and from 12 to 13. In Figure 16, the radiance reflectances estimated with

C2R at Sites 1 and 2 are similar to the in situ radiance reflectance. They also have the same level as the in situ radiance reflectance. At Site 3, the result is not as good. At short wavelengths, the C2R gives too large values. Still the water leaving radiance reflectance is in better agreement with the in situ radiance reflectance than the 6SV radiance reflectance. In [55], Koponen et al. found that even better results are achieved when ICOL (Improved Contrast between Land and Ocean) processor is used before the atmospheric correction. ICOL processor decreases adjacency effect.

The difference between the radiance reflectances estimated with 6SV and with the atmospheric correction of MERIS Lakes processors is quite large. One of the main reasons for this might be the faults in the aerosol modelling of 6SV which were described in Section 4.3. Also 6SV does not take into account algae foam and cirrus clouds effect on the TOA radiance, unlike the atmospheric correction of MERIS Lakes processors

The adjacency effect might be taken into account in a better way in the atmospheric correction of MERIS Lakes processors. 6SV takes into account the adjacency effect by setting all pixels around the target to the same value defined by the environment type which is set by the user. This might not be enough accurate method for the lake water atmospheric correction where the measurements are greatly affected by the areas around the lake.

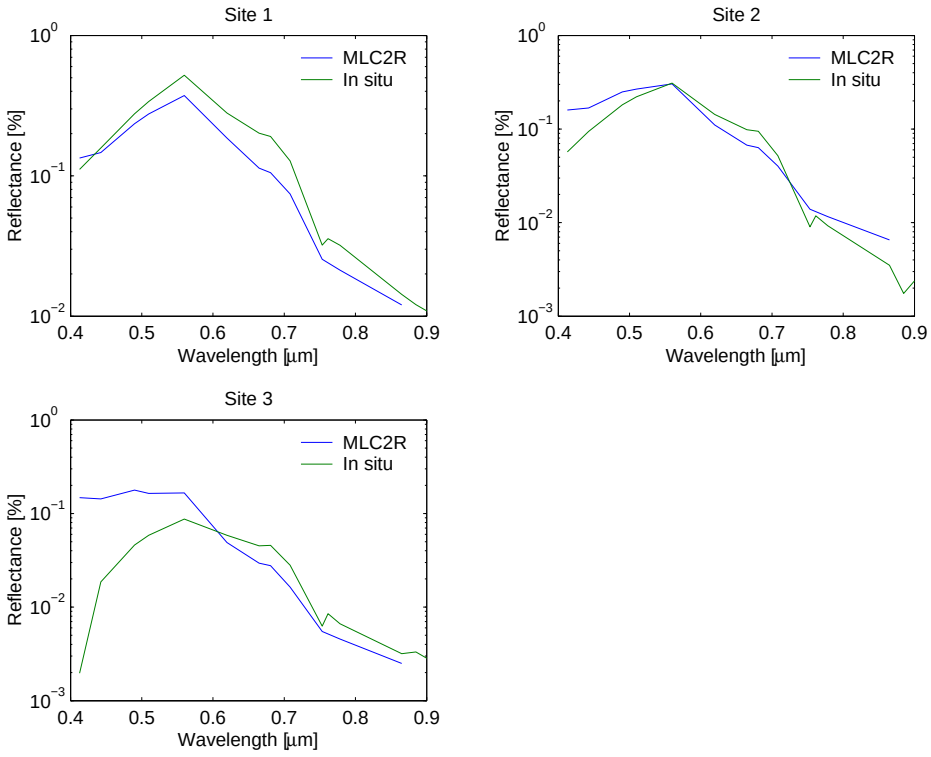

Figure 16: Water leaving radiance reflectance estimated with C2R processor from MERIS data product of 7th of August 2007 at three sites of Lake Päijänne area at MERIS Channels from 1 to 10 and from 12 to 13. At Sites 1 and 2, the estimation fits well to the in situ radiance reflectance measured on the same day. At Site 3 the estimate is not as accurate.

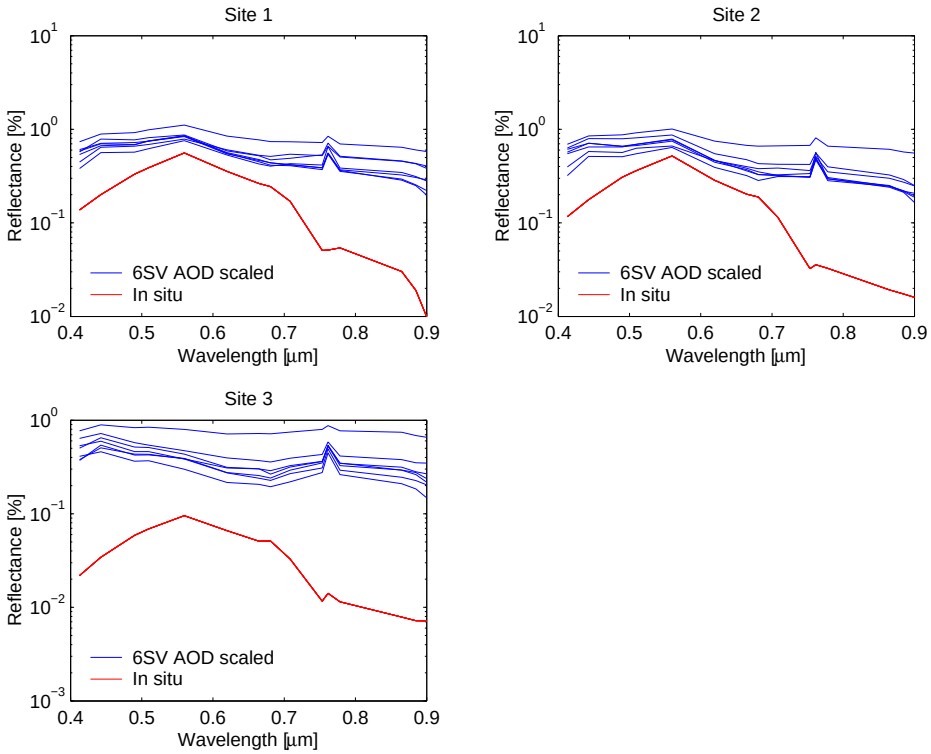

Figure 17: Water leaving radiance reflectance estimated with 6SV on seven days between 1st and 8th of June 2007. In the estimation, AOD values were scaled according to the in situ measurement at Jokioinen. The in situ radiance reflectances is from 4th of June 2007.

4.5 The effects of atmospheric corrections on the variation of satellite signal

It was studied if the atmospheric correction code based on 6SV or the atmospheric correction of Case-2 Regional processor (C2R) decreases the variation in satellite measurement caused by the atmosphere. The following procedure was executed. Seven satellite images from eight days period between 1st of June and 8th of June 2007 were corrected with both atmospheric correction methods. 6SV was used with and without scaling of AOD. During this eight days period, the water leaving radiance reflectance should not change much. However, the atmosphere's parameters will change. In Figure 17, there are seven AOD scaled atmospheric corrections made with 6SV. In Figure 18 the surface reflectances for the same period estimated with atmospheric correction of C2R processor are shown. The figures also presented the in situ radiance reflectance measured on 4th of June 2007. The same observations can be made from these corrections as were made from the corrections of 7th August 2007 data product. Water leaving radiance reflectances estimated with C2R processor are in better agreement with the in situ radiance reflectances than the radiance reflectances of 6SV.

Scaled standard deviation of the water leaving radiance reflectance was studied at

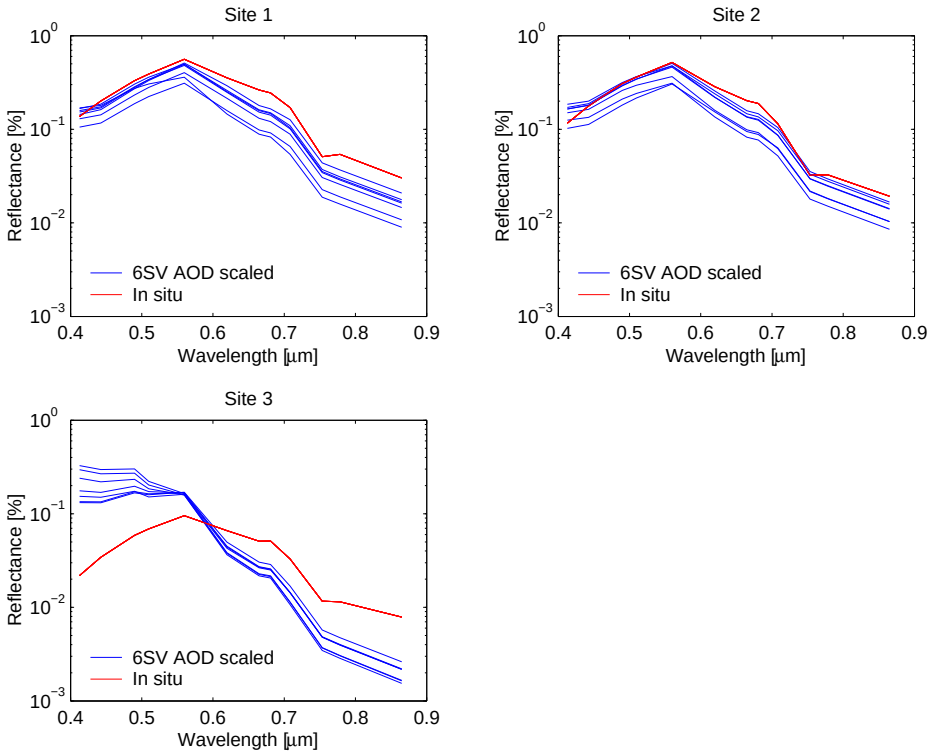

Figure 18: Water leaving radiance reflectance estimated with atmospheric correction of C2R processor on seven days between 1st and 8th of June 2007. The in situ radiance reflectance is from 4th of June 2007.

Site 1 on all channels. The usual standard deviation was scaled to be percentage of the channels mean by multiplying the standard deviation with $\frac{100\%}{\overline{\rho(\lambda)}}$. In this way, it was studied how large percentual variations are in the estimated water leaving radiance reflectance. The scaled standard deviation is

$$s(\lambda) = \left(\frac{1}{N-1} \sum_i \left(\rho(i,\lambda) - \overline{\rho(\lambda)} \right)^2 \right)^{\frac{1}{2}} \cdot \frac{100\%}{\overline{\rho(\lambda)}}, \tag{50}$$

where number of samples $N = 7$ and $\overline{\rho(\lambda)}$ is the mean of surface reflectance at wavelength λ. The scaled standard deviation was calculated for only one site to ensure that the radiance reflectance of the lake will not change much. The scaled standard deviations of TOA reflectance, 6SV radiance reflectance, AOD scaled 6SV radiance reflectance and C2R radiance reflectance are in Figure 19.

C2R processor has the largest scaled standard deviation at all MERIS channels and the 6SV without AOD scaling has the smallest. Allthough C2R processor's surface radiance reflectance's level and shape corresponds better to the in situ radiance reflectance, it does not decrease the percentual standard deviation of the radiance reflectance compared to the TOA reflectance or 6SV corrected radiance reflectance. The 6SV corrected radiance reflectance has smaller scaled standard deviation than the TOA reflectance's scaled standard deviation. We can also see that the scaling

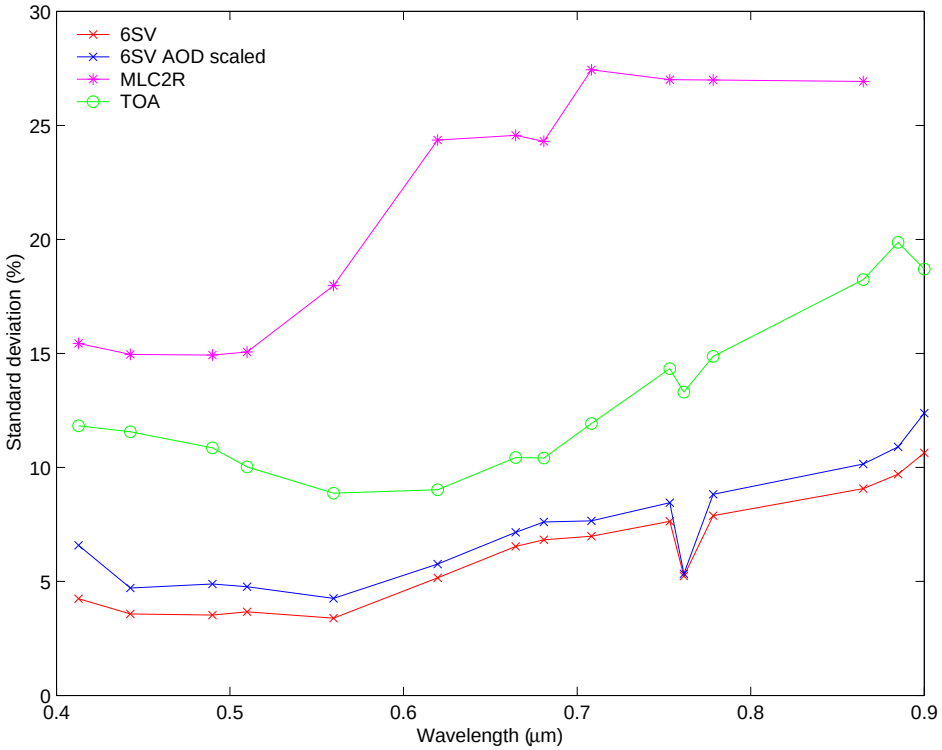

Figure 19: The scaled standard deviations of water leaving radiance reflectance estimates from seven days at Site 1 made with C2R processor, with 6SV without AOD scaling and with AOD scaling. The scaled standard deviation of TOA reflectance is also included.

of the AOD values with the in situ measurements does not decrease the variation of the radiance reflectance. The scaling of the AOD increases the absolute error to the in situ radiance reflectance and it increases the scaled standard deviation.

It might be that the scaled standard deviation is not a very good way to measure the variation of the satellite signal because low average values are punished hard. It may be so that the scaled standard deviation is more dependent on the average of the signal than on the variation of the signal. Radiance reflectance of C2R processor has the smallest average and it gets the largest scaled standard deviation too.

4.6 Water parameter estimation with the atmospherically corrected data

Radiance reflectances estimated with 6SV were used for the estimation of three bio-optical parameters with MERIS Lake Water Algorithm neural network. Figure 20 shows scatterplots of the estimated parameters and the in situ measurements made on the surface at time of the satellite's overpass. The atmospheric correction has been made with and without the AOD scaling. The water parameters estimated from both corrections are shown in the figure. From both corrections, the absorp-

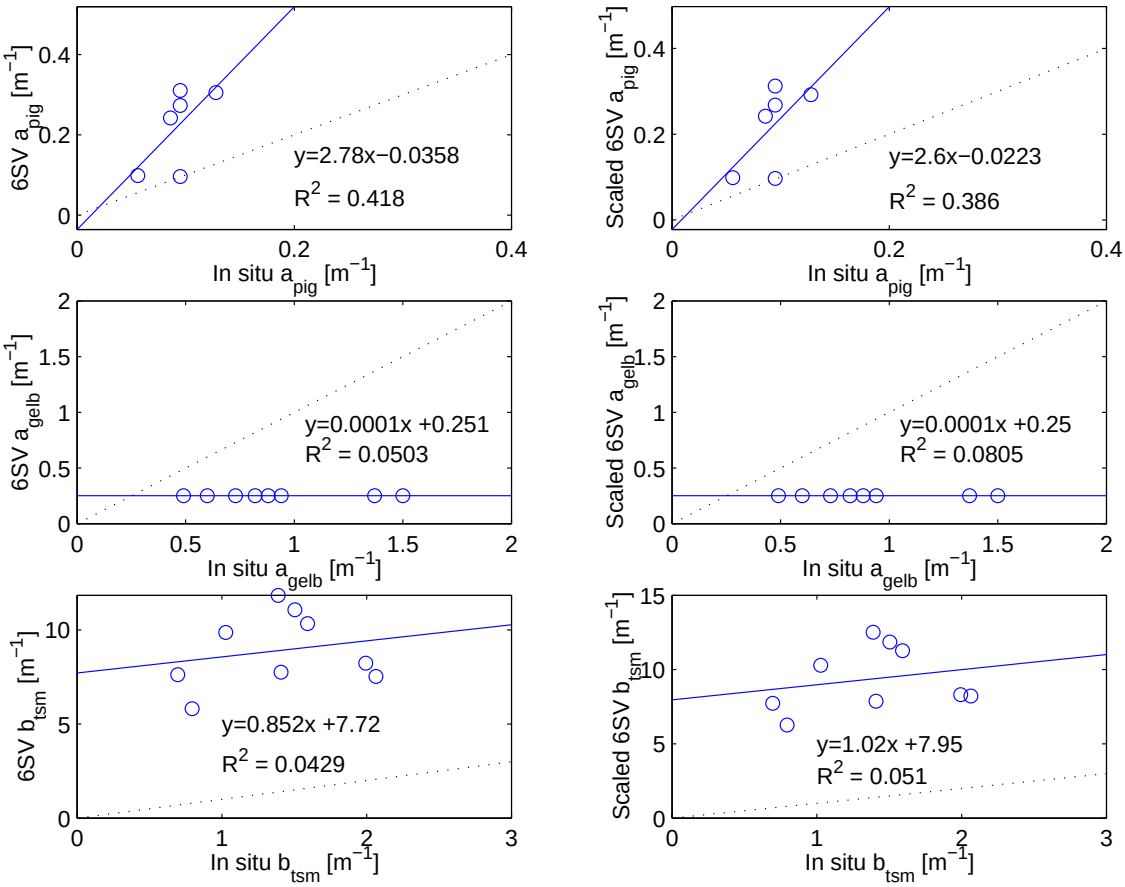

Figure 20: Water parameters derived from 6SV atmospheric corrected data with and without AOD scaling. Scatterplots for absorption coefficient of phytoplankton pigment a_{pig}, absorption coefficient of dissolved organic matter a_{gelb} and scattering from all particles b_{tsm}. All parameters are estimated or measured at MERIS Channel 2. On the x-axis is the value of in situ measurement and on the y-axis is estimate derived from the 6SV corrected data. The atmospheric correction is made with and without the scaling of AOD values. Dotted line is the 1:1 line. Regression equations and coefficients of determination are also given.

tion coefficient of dissolved organic matter a_{gelb} has been estimated to 0.25 m^{-1} with all samples. This is the minimum value of MERIS Lake Water Algorithm's output. Regardless of the in situ measurement's value, a_{gelb} is estimated to the same value. With the absorption coefficient of phytoplankton pigment a_{pig} and scattering coefficient of all particles b_{tsm}, the situation is a bit better. AOD scaling seems to have only a small effect on the scatterplots. Scatterplots of both 6SV corrections are very similar.

Regression equations and coefficients of determination R^2 were calculated for water parameters. The values for both 6SV corrections are presented in Figure 20 and in Table 8. The slope of a_{gelb}'s regression equation and coefficient of determination are small for both 6SV data. The slope of a_{pig} is better with both 6SV data. Also

Table 8: Regression equation and coefficient of determination R^2 for the water parameters based on three different atmospheric corrections. In the regression equations, x is the in situ measurement of the parameter and y is the estimated value. Values for MERIS Lakes Boreal processor are from [55].

Correction	**Parameter**	**Regression equation**	R^2	N
6SV	a_{pig}	$y = 2.8x - 0.04$	0.41	6
	a_{gelb}	$y = 0.0001x + 0.25$	0.05	9
	b_{tsm}	$y = 0.85x + 7.72$	0.04	9
6SV AOD scaled	a_{pig}	$y = 2.6x - 0.02$	0.39	6
	a_{gelb}	$y = 0.0001x + 0.25$	0.08	9
	b_{tsm}	$y = 1.02x + 7.95$	0.05	9
ML Boreal	a_{pig}	$y = 0.78x - 0.13$	0.09	7
processor	a_{gelb}	$y = 0.174x + 0.13$	0.44	9
	b_{tsm}	$y = 1.25x - 0.72$	0.72	11

the coefficient of determination is much better. For the b_{tsm}, the slope is close to 1, especially with AOD scaled 6SV data. However, its regression equation has a big offset value. Also, the coefficient of determination gets small value due the dispersion of the data.

Koponen et al. studied these same three parameters with MERIS Lakes Boreal processor, one of MERIS Lakes processors. They also used the same MERIS data and in situ radiance reflectance as it was used here. Their results for regression equations and coefficients of determination originally presented in [55] are in Table 8. For the a_{gelb} and b_{tsm}, the coefficient of determination is significantly better for MERIS Lakes Boreal processor than for 6SV. However, the coefficient of determination for a_{pig} is better for the 6SV atmospheric correction. Overall, 6SV based atmospheric correction does not give good results. MERIS Lakes Boreal processor gives clearly better results.

The main reason why the water parameters are estimated wrong is that the surface reflectance estimated with 6SV does not correspond to the real situation. Also it might be that the MERIS Lake water algorithm has learned the features of atmospheric correction of MERIS Lake processors, also its flaws. This makes it unsuitable to be used with other atmospheric correction methods.

4.7 Correlation with the in situ data

It was studied if the atmospheric correction code increases the linear relationship between the satellite data and the in situ radiance reflectance of water surface. Correlation coefficients were calculated between the in situ radiance reflectance and the 6SV based atmospheric corrections, and between the in situ radiance reflectance and the TOA reflectance at every MERIS channel. They are shown in Figure 21. The

in situ data have nine samples. They were collected on three days, 4th of June, 8th of August and 23rd of August 2007, at three locations on each day. All correlation coefficients decrease when the wavelength increases. This is suprising, because at longer optical wavelengths, atmosphere has smaller effect on the satellite signal. This can be seen for example from Figure 12 by comparing the TOA reflectance and the in situ radiance reflectance. However in this case, the decrease of the correlation coefficient is due to smaller variance of the in situ radiance reflectance at longer wavelengths. At longer wavelengths, the in situ radiance reflectance samples are more close to each other than at shorter wavelengths. This can be seen from Appendix B, where are the scatterplots of in situ radiance reflectance and TOA reflectance at all MERIS channels. Because at longer wavelengths the in situ radiance reflectance gets almost the same value in all sample points the linear dependency between the TOA reflectance and the in situ radiance reflectance cannot be seen. This causes small correlation coefficients at longer wavelengths. A correlation coefficient at one channel should not be compared to a correlation coefficient at another channel. However, we still can compare correlation coefficients at the same channel. At short wavelengths, the correlation coefficients of atmospherically corrected data are better than the correlation coefficients of TOA reflectance. At longer wavelengths the correlation coefficients of TOA reflectance are better. This indicates that atmospheric correction could be usefull at shorter wavelengths, where the effect of scattering is larger. It can be seen as well that the AOD scaling in the atmospheric correction increases the correlation coefficient at all wavelengths.

Next it was studied if the 6SV atmospheric correction increases the correlation between the satellite data and the in situ measurements of water quality parameters. The water quality parameters included concentration of chlorophyll-a, turbidity, concentration of total suspended matter and Secchi depth. The in situ data have nine samples for every water quality parameter and they have been measured on the same three days and at the same three sites as the in situ radiance reflectances were measured. The values of the water quality parameters can be seen in Table 6. The results are presented in Figure 22. The correlation coefficients of turbidity, total suspended matter and Secchi were found become clearly better when the atmospheric correction is executed. Again, the scaling of the AOD values seems to increase the correlation between the in situ data and the satellite data. The concentration of chlorophyll-a correlate better with the uncorrected satellite data than with the atmospherically corrected satellite data. The reason why the atmospheric correction decreases the correlation coefficient of chlorophyll-a concentration, might be that there is a nonlinear relation between the chlorophyll-a concentration and the surface reflectance. Equation (47) points also to this direction.

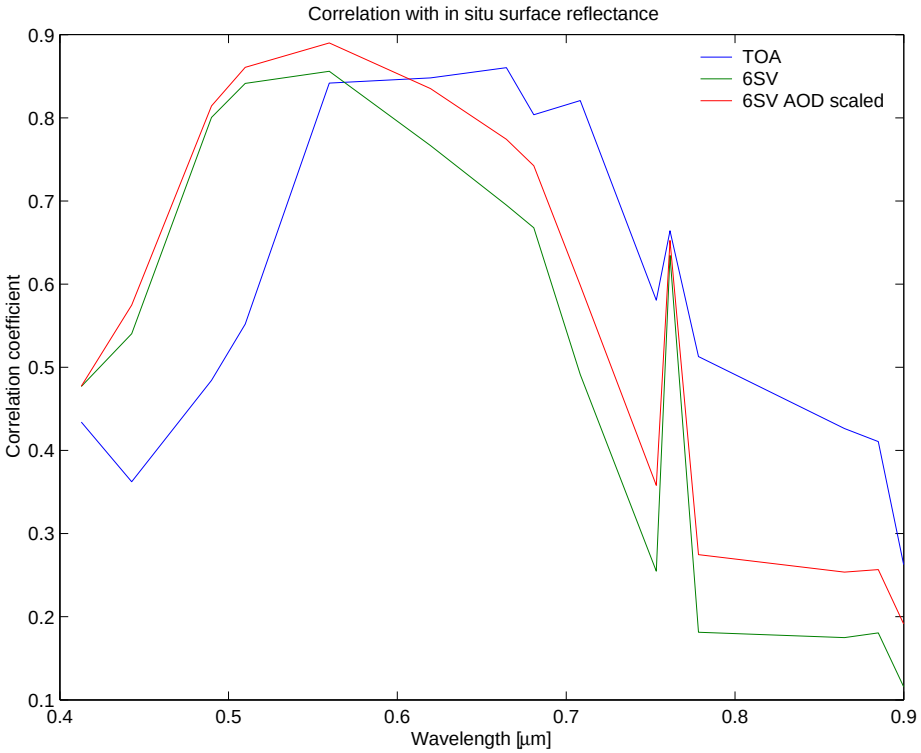

Figure 21: In situ radiance reflectance's correlation with TOA reflectance, 6SV radiance reflectance and AOD scaled 6SV radiance reflectance. Nine in situ reflectance samples were taken on three days in summer 2007 at three locations on each day.

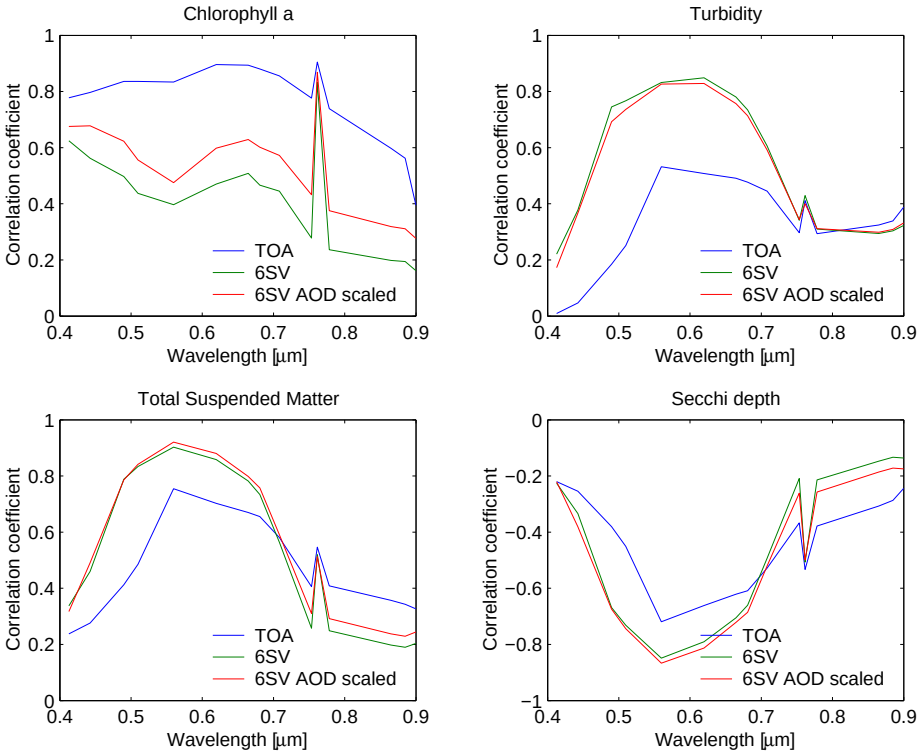

Figure 22: Water quality parameters' correlation with satellite data. The water quality parameters include chlorophyl-a concentration, turbidity, concentration of total supended matter and Secchi depth. The satellite data include TOA radiance, 6SV radiance reflectance and AOD scaled 6SV radiance reflectance. The water quality parameters have nine samples taken on three days in summer 2007 at three locations on each day. The 6SV atmospheric correction increases satellite data's correlation with turbidity, concentration of total suspended matter and Secchi depth, but not with chlorophyll-a concentration.

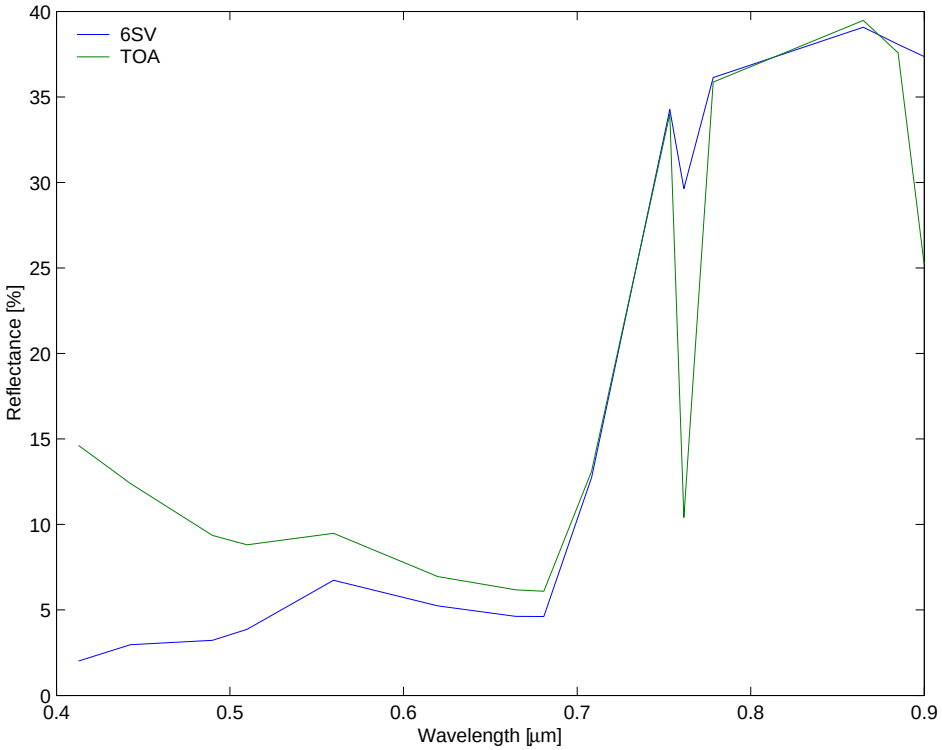

Figure 23: 6SV estimated surface reflectance on land on 7th of August 2007 and the corresponding TOA reflectance.

4.8 Atmospheric correction code on land surface

Out of curiosity, the effect of the 6SV based atmospheric correction on a satellite measurement on land surface was studied. Figure 23 shows the 6SV estimated surface reflectance of a land pixel and the corresponding TOA reflectance. The atmospheric correction decreases the reflectance more at the shorter than at the longer wavelengths. This is expected because exponential behavior of scattering of the atmosphere. Also the absorption line at Channel 11 is corrected to the right direction. It remains open how well the atmospheric correction code based on 6SV works on land surface, because of the lack of validation data from land surface. However, the atmospheric correction made here does not exclude the possibility that the code could be used successfully on a land surface.

5 Summary

In this Master's thesis methods for the atmospheric correction of satellite measurements of Finnish lakes were studied. The atmospheric correction code makes atmospheric correction to MERIS Level 1 radiance data by using 6SV radiative transfer code with atmospheric satellite data products. It calculates atmospheric correction parameters at the points of a grid set on the satellite image. It interpolates atmospheric correction in all pixels of the image. The surface reflectance estimated with the code was compared to the in situ radiance reflectance from Finnish lakes.

In the validation of atmospheric correction code the 6SV estimated surface radiance reflectances were seen to be clearly larger than the in situ radiance reflectances. AOD was found to have crucial effect on the atmospheric correction. AOD is by far the most important input parameter for the atmospheric correction. Also, it was found that scattering dominates the detected radiance at short optical wavelengths. To get more accurate measurements of the AOD, the satellite measurements of AOD were scaled with in situ measurement from weather station. The scaling of AOD gave even larger absolute error compared to the in situ radiance reflectance.

The 6SV corrected radiance reflectances were found to be unsuitable input for the MERIS Lake Water Algorithm. However, it was seen that the atmospheric correction increases satellite data's correlation with turbidity, total suspended matter and Secchi depth. With the AOD scaling the correlation increases even more. The atmospheric correction did not increase the correlation between the satellite data and chlorophyll-a concentration.

One of the main reasons for the failure of the atmospheric correction might be the inaccurate AOD satellite data. According to Doerffer [44] AOD data should be taken from the data product to be corrected. The atmospheric correction code uses AOD data from MODIS satellite instrument. Because of this AOD data do not have exactly the same location and time as the data to be corrected. This decreases the quality of the atmospheric correction. Also the pixel size of MODIS aerosol data product is larger than the pixel size of the MERIS data product. The accuracy of the computation grid might be too small. However, because of the time needed for the computations of 6SV radiative transfer code (4h for a whole MERIS image), it is not reasonable to increase the accuracy of the computation grid.

The aerosol model of 6SV might not be accurate enough for the atmospheric correction of water measurement. At the satellite the path radiance from the atmosphere can be more than 10 times larger than the radiance from water [60]. This makes the atmospheric correction of water reflectance very sensitive to errors in the atmospheric correction, which in turn is sensitive to the aerosol modelling. However, only AOD was fed to the 6SV radiative transfer code. No information on the spectral behavior of the aerosols was used with 6SV. Another shortcoming of 6SV's aerosol modelling is that it is not modified to the atmosphere of Finland.

The atmospheric correction of MERIS Lakes processors was compared to the 6SV based atmospheric correction. It clearly gave smaller absolute error to the validation

data than 6SV. It was also found to be more suitable as the input of MERIS Lake Water Algorithm. All in all, for the estimation of water surface reflectance the atmospheric correction of MERIS Lakes processors was found to be better than the 6SV based atmospheric correction.

Because of the lack of validation data from land surface, it remains open how well the atmospheric correction code based on 6SV works on a land surface. However, in the future, it could be interesting to see if the code could be used on remote sensing of land.

References

[1] Rees, W.G., Physical principles of remote sensing 2nd edition, Cambridge University Press, 2001

[2] Vermote, E.F., Tanré. D.,Herman, M., Morcrett, J.J., Kotchenova, S.Y., Second simulation of the satellite signal in the solar spectrum, 6S user guide version 3, November 2006, [Online] Available at `http://6s.ltdri.org`

[3] MERIS Product Handbook, Issue 2.1, 24 October 2006, European Space Agency, 2006

[4] Ikonen, E., Optiikan perusteet, Espoo, Helsinki University of Technology, 2006

[5] Koponen, S., Remote sensing of water quality for Finnish lakes and coastal areas, Dissertation for the Degree of Doctor of Science in Technology, Espoo, Helsinki University of Technology, Department of Electrical and Communications Engineering, 2006

[6] Schanda, E., Physical fundamentals of remote sensing, Springer, 1986

[7] Harrison, R.M (editor), Understanding our environment - an introduction to environmental chemistry and pollution 3rd edition, Royal Society of Chemistry, 1999, pp. 19-12

[8] Karttunen, H., Koistinen, J, Saltikoff, E, Manner, O, Ilmakehä ja sää, Helsinki, Tähtitieteellinen yhdistys Ursa, 1997

[9] Masson, P.J., Thompson, D.J., Boundary layers, Encyclopedia of atmospheric sciences, Elsevier, 2003, pp. 221

[10] Vermote, E.F., Tanré, D., Deuze, J.L., Herman, M., Morcrett, J.J., Second simulation of the satellite signal in the solar spectrum, 6S: an overview. IEEE Transactions on Geoscience and Remote Sensing, 1997, Vol. 35, pp. 675-686

[11] Elachi, C., van Zyl, J., Introduction to the physics and techniques of remote sensing, John Wiley & Sons, Inc., 2006

[12] Astrossp web page, (June 2008), http://haro.astrossp.unam.mx/∼hiriart/radiometro/html-files/pwv-definition.html

[13] Seinfeld, J.H., Spyros, N.P., Atmospheric chemistry and physics, John Wiley & Sons Inc., 2006

[14] Renzullo, L. J., Radiometric processing of multitemporal sequence of satellite imagery for surface reflectance retrievals in change detection studies, Doctor of Philosophy thesis, Curtin university of technology, Australia, 2004, Available at http://adt.curtin.edu.au/theses/available/adt-WCU20050222.162402/unrestricted/

[15] Robles Gonzáles, C., Retrieval of aerosol properties using ATSR-2 observations and their interpretation, Doctor of Philosophy thesis, University of Utrecht, 2003

[16] Collins, D.G., Blattner, W.G., Wells, M.B., Horak, H.G., Backward Monte Carlo calculations of the polarization characteristics of the radiation emerging from spherical-shell atmospheres, Applied Optics, 1972, Vol. 11, No. 11, pp. 2684-2696

[17] Mélin, F., Zibordi, G., Djavidnia, S., Development and validation of a technique for merging satellite derived aerosol optical depth from SeaWiFS and MODIS, Remote Sensing of Environment, 2007, Vol. 108, pp. 436-450

[18] Mather, P.M., Computer processing of remotely-sensed images - an introduction 3rd edition, John Wiley & Sons, 2004

[19] Bates, D.E., Porter, J.N., AO3D: A Monte Carlo code for modeling of environmental light propagation, Journal of Quantitative Spectroscopy & Radiative Transfer, 2008, Vol. 109, pp. 1802-1814

[20] Popp, T., Correcting atmospheric masking to retrieve the spectral albedo of land surfaces from satellite measurements, International Journal of Remote Sensing, 1995, Vol. 16, pp. 3843-3508

[21] Kotchenova, S.Y., Vermote, E.F., Levy, R., Lyapustin, A., Radiative transfer codes for atmospheric correction and aerosol retrieval: intercomparison study, Applied Optics, 2008, Vol. 47, No. 13, pp. 2215-2226

[22] Shettle, E.P., Weinman, J.A., The transfer of solar irradiance through inhomogeneous turbid atmospheres evaluated by Eddington's approximation, Journal of atmospheric sciences, 1970, Vol. 27, pp. 1048-1055

[23] Garcia, R.D.M, Siewert, C.E., On discrete spectrum calculations in radiative transfer, Journal of Quantitative Spectroscopy & Radiantive Transfer, 1989, Vol. 42, pp. 385-394

[24] Liou, K.N., A numerical experiment on Chandrasekhar's discrete-ordinate method for radiative transfer: application to cloud and hazy atmospheres, Journal of Atmospheric Sciences, 1973, Vol. 30, pp. 1303-1326

[25] Stammes, K., Tsay, S. E., Wiscombe, W., Jayaweera, K., A numerically stable algorithm for discrete-ordinate-method radiative transfer in multiple scattering and emitting layered media, Applied Optics, 1988

[26] Benassi, M., Garcia, R.D.M., Karp, A.H., Sievert, C.E., A high-order spherical harmonics solution to the standard problem in radiative transfer, The Astrophysical Journal, 1984, Vol. 280, pp. 853-864

[27] Kneizys, F.X., Shettle, E.P., Abreu, L.W., Chetwynd, J.H., Anderson, G.P., Gallery, W.O., Selby, J.E.A., Clough, S.A., Users guide to LOWTRAN 7, Hanscomb Air Force Base, U.S. Air Force Geophysics Laboratory, 1988, pp. 137

[28] Berk, A.L., Anderson, G.P., Bernstein, L.S., Acharya, P.K., Dothe, H., Matthew, M.W., Adler-Golden, S.M., Chetwynd, J.H.J., Richtsmeier, S.C., Pukall, B., Allred, C.L., Jeong, L.S., Hoke, M.L., MODTRAN4: Radiative transfer modelling for atmospheric correction, AVIRIS Proceedings 1999 (JPL Publication 99-17). Pasadena, CA.: NASA Jet Propulsion Laboratory, 1999

[29] Gao, B.-C., Heidebrecht, K.B., Goetz, A.F.H, Derivation of scaled surface reflectances from AVIRIS data, Remote Sensing of Environment, 1993, Vol. 44, pp. 145-163

[30] Tanré, D., Deroo, C., Duhaut, P., Herman, M., Morcrette, J.J., Perbos, J., Deschamps, P.Y., Simulation of the satellite signal in the solar spectrum, Universite des Sciences et Techniques de Lille, Laboratoire d'Optique Atmospherique, 1986

[31] Modtran 4 software web page, (July 2008), Kirtland US Air Force, `http://www.kirtland.af.mil/library/factsheets/factsheet.asp?id=7915`

[32] Cornette, W. M, Using the MOSART code for atmospheric correction, Geoscience and Remote Sensing Symposium, IGARSS '94, 1994

[33] Nordlund, K., Course material for the Monte Carlo simulations course at Helsinki University, 2006

[34] Bréon, F.-M., Reflectance of a broken cloud fields: simulation and parametrization, Journal of Atmospheric Sciences, 1992, Vol. 49, pp. 1221-1232

[35] Arino, O., Vermote, V., Spaventa, V., Operational atmospheric correction of Landsat TM imaginary, Earth Observation Quarterly, 1997

[36] Zhao, W., Tamura, M., Takashi, H., Atmospheric and spectral corrections for estimating surface albedo from satellite data using 6S code, Remote sensing of environment, 2000, Vol. 76, pp. 202-212

[37] Vermote, E.F, El Saleous, N.Z., Justice, C.O., Atmospheric correction of MODIS data in the visible to middle infrared: first results, Remote Sensing of Environment,2002, Vol. 83, pp. 97-111

[38] Floricioiu, D., Rott, H., Atmospheric correction of MERIS data over perialpine lakes, MERIS-(A)ATSR Workshop, Frascati, Italy, ESA, 2005

[39] Radiative transfer code comparison web page of the MODIS atmospheric correction group, (July 2008), `http://rtcodes.ltdri.org/Main_simple.htm`.

[40] Kotchenova, S.Y., Vermote, E.F., Matarrese, R., Klemm, F.J. Jr., Validation of a vector version of the 6S radiative transfer code for atmospheric correction of satellite data. Part I: Path radiance, Applied Optics, 2006, Vol. 45, No. 26, pp. 6762-6774

[41] HITRAN web page, (July 2008), `http://www.hitran.com`.

[42] Goody, R.M., Atmospheric radiation: 1. Theoretical basis, Oxford University Press, 1964, pp. 436

[43] Malkumus, W, Random Lorentz band model with exponential-tailed S^{-1} line-intensity distribution function, Journal of the Optical Society of America, 1967, Vol. 57, No. 3, pp. 323-329

[44] Doerffer R., Schiller, H., ATBD MERIS regional coastal and lake case 2 water project - atmospheric correction, Version 1.0, 18th of May 2008, Geesthacht, Germany, GKSS Research Center, 2008

[45] Lindell, T., Pierson, D., Premazzi, G., Zilioli, E. (editors), Manual for monitoring European lakes using remote sensing techniques, Luxemburg, Office for Official Publications of European Communities, 1999

[46] Kirk, J.T.O., Light and photosynthesis in aquatic ecosystems, Cambridge University Press, 1994

[47] Ylöstalo, P., Kallio, K., Seppälä, J., Absorption properties of different in-water constituents of lake waters Manuscript, 2008

[48] Kallio, K., Pulliainen, J., Ylöstalo, P. MERIS, MODIS and ETM+ channel configurations in the estimation of lake water quality from subsurface reflectance with semi-analytical and empirical algorithms, 2005, Geophysica, Vol. 41, pp. 31-55

[49] Kallio, K., Optical properties of Finnish lakes estimated with simple bio-optical models and water quality monitoring data, Nordic Hydrology, 2006, Vol. 37, pp. 183-204

[50] Kondratyev, K.Y., Radiation in the atmosphere, N.Y. 10003, USA, Academic Press, 1969

[51] Doerffer R., Schiller, H., ATBD MERIS lake water algorithm for BEAM, Version 1.0, 10th of June 2008, Geesthacht, Germany, GKSS Research Center, 2008

[52] ESA Earthnet: ENVISAT web page, (August 2008), `http://envisat.esa.int/`.

[53] ESA Earthnet: Envisat still going strong after five successful years, (June 2008), Available at `http://www.esa.int/esaCP/SEM129N0LYE_index_0.html`

[54] Envisat 3D Navigator, (June 2008), Available at http://envisat.esa.int/object/index.cfm?fobjectid=1692

[55] Koponen, S., Ruiz-Verdu, A., Heege, T., Heblinski, J., Sorensen, K., Kallio, K., Pyhälahti, T., Doerffer, R., Bronckmann, C., Peters, M., Development of MERIS lake water algorithms: validation report, 2008, Available from http://www.brockmann-consult.de/beam-wiki/display/LAKES

[56] Modis web page, (August 2008), http://modis.gsfc.nasa.gov

[57] Aura EOS satellite system's web page, (September 2008), http://aura.gsfc.nasa.gov

[58] OMI web page of The Royal Netherlands Meteorological Institute, (September 2008), http://www.knmi.nl/omi

[59] ASD Inc.'s web page, (June 2008), http://www.asdi.com

[60] Behnert, I., Volker, M., Doerffer, R., Aerosol climatology from ground-based measurements for the southern North Sea, Atmospheric Research, 2007, Vol. 84, pp. 201-220

[61] Pyhälahti, T., E-mail conversation, 17th of July 2008

Appendix A: Documentation of the atmospheric correction code

A.1 ACC.M

Function

Makes atmospheric correction for MERIS level 1 or MODIS data i.e. it estimates the surface irradiance reflectance based on the radiance measured at the top of the atmosphere. The atmospheric correction is made with 6SV radiative transfer code and atmospheric satellite data. It utilizes MODIS aerosol product (MOD04), MODIS precipitable water vapor product (MOD05), OMI ozone product (OMTO3) and AOD measurements from the Earth's surface.

Usage

```
DATA  =  ACC( RAD_FILENAME, MODIS_GEO_FILENAME, MOD04_FILENAME,
MOD05_FILENAME, OMI_FILENAME, CHANNELS, ROI_ARG,
ROI_UPPER_LEFT_ROW, ROI_UPPER_LEFT_COL, ROI_UPPER_RIGHT_ROW,
ROI_LOWER_RIGHT_COL, AOD_IS, LAT_AOD_IS, LONG_AOD_IS )
```

Inputs

- `RAD_FILENAME`, the filepath of MERIS or MODIS radiance data.
- `MODIS_GEO_FILENAME`, the filepath of geolocation file of MODIS data. If not using MODIS data, argument should be set as empty array, `[]`.
- `MOD04_FILENAME`, `MOD05_FILENAME` are `OMI_FILENAME` filepaths of MODIS aerosol product, MODIS water vapor product and OMI ozone product, respectively. The `ACC` can be used with constant AOD, water vapor or ozone value. If the filename is set to numerical value, the value will be used in all points of the correction.
- `CHANNELS` is a vector giving the channels of the radiance product to be corrected.
- `ROI_ARG` is a string describing the format of the coordinates of Region Of the Interested. If `ROI_ARG='map'`, the coordinates of ROI are map coordinates. If `ROI_ARG='pix'` the coordinates are pixel coordinates.
- `ROI_UPPER_LEFT_ROW, ROI_UPPER_LEFT_COL, ROI_UPPER_RIGHT_ROW,` and `ROI_LOWER_RIGHT_COL` are coordinates in the image which define the area where the atmospheric correction is made. The coordinates can be pixel coordinates or map coordinates depending on `ROI_ARG`. The image's upper left

corner pixel coordinate is (1,1). When map coordinates are used the row in the name of the coordinate refers to longitude and col refers to the latitude of the location. If the atmospheric correction is made to the whole image, the ROI coordinates should still be given, at least as empty arrays.

- `AOD_IS`, in situ measurement of AOD. If `AOD_IS, LAT_AOD_IS` and `LONG_AOD_IS` are given the AOD values are scaled according to `AOD_IS`. If they are not given the code is ran without the AOD scaling.
- `LAT_AOD_IS` and `LONG_AOD_IS`, map coordinates of the in situ measurement.

Output

`DATA` is a structure with following fields:

- `DATA.rad_toa` is TOA radiance inside ROI.
- `DATA.rho_toa` is TOA reflectance inside ROI.
- `DATA.rho_6s` is surface reflectance estimated with 6SV inside ROI.
- `DATA.LAT` is latitudes of the pixels inside ROI.
- `DATA.LONG` is longitudes of the pixels inside ROI.
- `DATA. V_ZEN` is view zenith angles of the pixels inside ROI.
- `DATA.V_AZI` is view azimuth angles of the pixels inside ROI.
- `DATA.S_ZEN` is sun zenith angles of the pixels inside ROI.
- `DATA.S_AZI` is sun azimuth angles of the pixels inside ROI.
- `DATA.XA_tp` is atmospheric correction parameter xa at the computation grid.
- `DATA.XB_tp` is atmospheric correction parameter xb at the computation grid.
- `DATA.XC_tp` is atmospheric correction parameter xc at the computation grid.
- `DATA.AOD_used` is AOD measurements at the computation grid.
- `DATA.AOD_lat_used` is latitudes of the AOD measurements.
- `DATA.AOD_long_used` is longitudes of the AOD measurements.
- `DATA.water_vapor_used` is water vapor measurements at the computation grid.
- `DATA.water_vapor_lat_used` is latitudes of the water vapor measurements.
- `DATA.water_vapor_long_used` is longitudes of the water vapor measurements.

- `DATA.ozone_used` is ozone measurements at the computation grid.
- `DATA.ozone_lat_used` is latitudes of the ozone measurements.
- `DATA.ozone_long_used` is longitudes of the ozone measurements.
- `DATA.prod_info` is structure from `READPRODUCT.M` function containing information of the MERIS product.
- `DATA.sf_aod` is scale factor of the AOD scaling.

Description

1. `ACC.M` reads MERIS product with `READPRODUCT.M` function. MODIS radiance data and MODIS geolocation file are read with `READ_MOD02.M` function.
2. ROI map coordinates are converted to pixel coordinates with function `MAP2PIXEL.M` function.
3. Auxiliary data of the satellite product is interpolated from the tie points to all pixels with the help of `INTERPOLATION_IN_ROI.M` function.
4. Radiance inside ROI is cut from the whole image.
5. Atmospheric satellite data is red or a constant value is set. The data is red with functions, `READ_MOD04.M, READ_MOD05.M` and `READ_OMI.M`.
6. The computation grid is created. Every second tie point of MERIS product is taken starting from the upper left corner of the ROI. Also the the most right and the lowest tie point inside the ROI is selected.
7. The AOD, water vapor and ozone measurements are taken to the computation grid from the nearest points of the computation point for this it is used function `VALUE_FROM_GRID.M`.
8. If in situ measurement of AOD and it is location is given, the values of the aerosol product are scaled. The scaled AOD value is given by equation

$$\tau_{AOD,s} = \frac{\tau_{AOD,insitu}}{\tau_{AOD}(i,j)} \cdot \tau_{AOD}, \tag{A1}$$

   where $\tau_{AOD,insitu}$ is the in situ measurement, $\tau_{AOD}(i,j)$ is the satellite data's value at location of in situ measurement and τ_{AOD} is the initial satellite data.
9. Unit coversion to the units of 6SV. Water vapor measurements are converted with function `CM2GCM2.M` and ozone measurements are divided with 1000 to convert from DU to cm $\cdot$ atm. Altitudes are converted from m to km and negative altitudes are set to zero.
10. Loop for writting 6SV input file, using 6SV and reading 6SV output file.

```
FOR i=1:number_of_computation_points
          write input file
          run 6SV
          read output file
END
```

The input file is written with function `WRITE_6S_INPUT.M`, 6SV is ran from the command line of the operation system and the output file is read with function `READ_6S_OUTPUT`. From the output file of 6SV is taken atmospheric correction parameters and the solar irradiance below the atmosphere.

11. Interpolation of the atmospheric correction parameter to all pixels of ROI and calculation the surface reflectance according of them.

A.2 READPRODUCT.M

Function

Reads MERIS full resolution, level 1B data product from N1-file. Gives radiance in the unit of $[\frac{\mu m}{m^2 \cdot nm \cdot sr}]$. Converts the indexing of the radiance data to start from upper left corner.

Inputs

- `FILENAME` of the MERIS N1-file.
- `CHANNELS` to be extracted.
- `STEP` 2x2 vector describing the accuracy where the data is read.

Outputs

- `DATA`, three dimensional matrix, which has the radiance data. The first two dimensions correspond the x and y pixel coordinates. The third dimension corresponds the channel of MERIS.
- `FLAGS` contains radiance data's quality control flags.
- `MPH`, Main Product Header.
- `SPH`,Specific Product Header
- `TPS`, three dimensional matrix for tie point data. It has following data: latitudes, longitudes, view zeniths angles, view azimuths angles, ozones, surface temperatures, sun zenith angles and sun azimuth angles.

– PROD_INFO is a structure containing auxiliary information of the MERIS product. It has folloving fields.

```
PROD_INFO.SAMPLES_PER_TP
PROD_INFO.LINES_PER_TP
PROD_INFO.ORBIT_RADIUS
PROD_INFO.SENSING_START
PROD_INFO.LINE_LENGTH
PROD_INFO.NUM_BANDS
PROD_INFO.INITIAL_WAVELEN [um]
PROD_INFO.FINAL_WAVELEN [um]
```

Description

The function is made by Ville Bergholm to his special assignment course in TKK's laboratory of Space Technology on 2003. More information of the function can be found from Ville Bergholm's written part of the special assignment course `http://users.tkk.fi/~vberghol`. The original function was modified for atmospheric correction so that the more data was added to the `TPS` matrix and `PROD_INFO` structure. Also the `FLAGS` matrix was added to the output. The radiance data was modified so that it is in agreement with MATLAB's way to handle images.

A.3 MAP2PIXEL.M

Function

To find corresponding pixel coordinates to given map coordinates in MERIS FR level 1b image.

Input

– `LONGITUDE` and `LATITUDE`, map coordinates, which we want to convert pixel coordinates.

– `TPS` tie point grids of the MERIS data.

– `SAMPLES_PER_TP` number of pixels between two tie points in a row (in across track).

– `LINES_PER_TP` number of pixels between two tie points in a column (in along track).

Output

– `ROW_COORD, COL_COORD`, pixel coordinates.

Description

The function finds dependency between map coordinates and pixel coordinates in MERIS FR level 1B product by fitting 1. degree two variable polynomial to the latitude and longitude tie point grids. From this polynomial it finds the pixel coordinates corresponding map coordinates.

A.4 INTERPOLATION_IN_ROI.M

Function

Interpolates MERIS tie point data inside box defined by the tie points next to the Region Of Interest.

Input

- `TP`, two dimensional tie point grid to be interpolated.
- `ROI_upper_left_row, ROI_upper_left_col, ROI_lower_right_row, ROI_lower_right_col`, Region Of Interest.
- `SAMPLES_PER_TP` number of pixels between two tie points in a row (in across track).
- `LINES_PER_TP` number of pixels between two tie points in a column (in along track).

Output

- `VALUES_IN_ROI` data interpolated to all pixels.
- `SS_UL_ROW, SS_UL_COL, SS_LR_ROW, SS_LR_COL` corners of the interpolated date in pixel coordinates of original image.
- `TP_UL_ROW, TP_UL_COL, TP_LR_ROW, TP_LR_COL` corners of the interpolated date in coordinates of tie point grid.

Description

The function finds the nearest corner up left from the ROI's upper left and the nearest corner down right from the lower right corner of ROI. This is illustrated in Figure A1. Then tie point grids data is interpolated to all pixels in side the extended ROI.

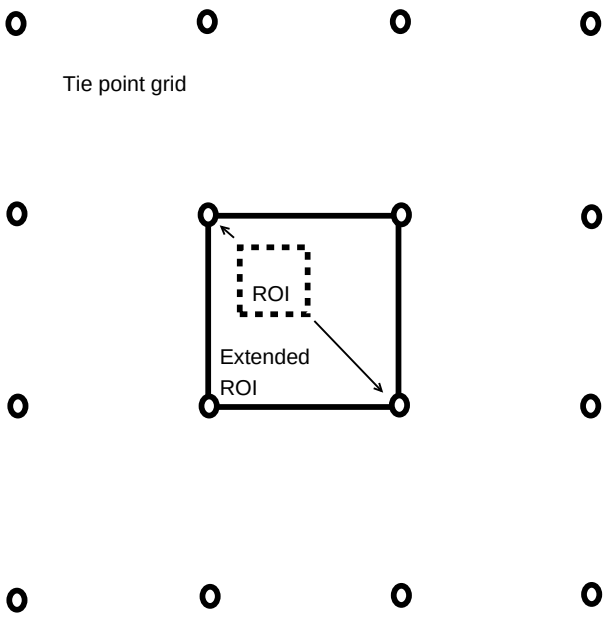

Figure A1: ROI is given as an input argument to the INTERPOLATION_IN_ROI.M function. The function finds the nearest corner up left from the ROI's upper left and the nearest corner down right from the lower right corner of ROI. Then tie point grids data is interpolated to all pixels in side the extended ROI.

A.5 READ_MOD04.M

Function

To read AOD and location data from MODIS aerosol product, MOD04, (HDF4 EOS file).

Input

– `FILENAME`, filepath of the MODIS aerosol product.

Output

– `AOD`, aerosol optical depth data from 'Optical_Depth_Land_And_Ocean' data set.

– `LATITUDES`, `LONGITUDES`, geolocalisation data.

Description

The function uses HDF functions of MATLAB.

A.6 READ_MOD05.M

Function

To read precipitable water vapor and location data from MODIS water vapor product, MOD05, (HDF4 EOS file).

Input

– `FILENAME`, filepath of the MODIS water vapor product.

Output

– `WATER_VAPOR`, precipitable water vapor data from .

– `LATITUDES`, `LONGITUDES`, geolocalisation data.

Description

The function uses HDF4 functions of MATLAB.

A.7 READ_OMI.M

Function

To read total column ozone from OMI OMTO3 file using HDF5 format.

Input

– `FILENAME`, filepath of the OMI total column ozone product.

Output

– `COLUMN_OZONE`, total column ozone data from data set 'ColumnAmountO3'.

– `LATITUDES`, `LONGITUDES`, geolocalisation data.

Description

Runs H5DUMP software from the command line of the operation system and `READ_HDUMP.M` function to read the output of HDUMP.

A.8 READ_HDUMP.M

Function

To read output of H5DUMP software from output file.

Input

– `FILENAME`, filepath of the data set ASCII file.

Output

– `M`, data set in a matrix.

A.9 VALUE_FROM_GRID.M

Function

To select nearest pixel to given location from latitude and longitude grid and returns corresponding pixel from matrix `A`.

Input

– `A`, matrix from where scalar is to be found.

– `lat, long`, geolocation corresponding the point to be found.

– `lat_grid, long_grid`, geolocation matrixes corresponding matrix `A`.

Output

– `a`, the value of `A` corresponding `lat` and `long`.

– `lat_used, long_used`, map coordinates of the `a`.

– `indx, indy`, pixel coordinates of the `a`.

Description

The function calculates sum of squares to the differences of latitudes and longitudes.

```
d=(lat_grid -lat).^2 + (long_grid -long).^2
```

After that it takes the indexes of the minimum value of `d` and returns value from matrix `A` with the indexes.

A.10 CM2GCM2.M

Function

To change the unit of total precipitable water from cm to g/cm^2 by multiplying input with density of water.

A.11 WRITE_6S_INPUT.M

Function

To write 6SV input file with given input arguments.

Input

- `V_ZEN, V_AZI, S_ZEN, S_AZI`, view zenith, view azimuth, sun zenith, sun azimuth.
- `ALTITUDE`, altitude of the target.
- `MONTH, DAY`, time of the satellite capture.
- `CHAN`, MERIS channel.
- `AOD`, Aerosol Optical Depth.
- `WATER_VAPOR`, precipitable water vapor.
- `OZONE`, total column ozone.
- `INPUT_FILENAME`

Description

Writes input file with continental aerosol model, non homogeneus surface, lake water target reflectance, green vegetation environment, 1 km target and for Lambertian surface.

A.12 READ_6S_OUTPUT.M

Function

To read atmospheric correction parameters and downwelling surface irradiance from 6SV output file.

Appendix B: Scatterplots of in situ radiance reflectance and TOA reflectance

In Figure B1 are scatterplots of TOA reflectance and in situ radiance reflectance at all MERIS channels. The in situ radiance reflectances are measured on three days during summer 2007, as was described in Section 3.5. The TOA radiances are measured on the same days over the same locations by MERIS satellite instrument. Because at longer wavelengths the in situ radiance reflectance gets almost the same value in all sample points a linear dependency between the TOA reflectance and the in situ radiance reflectance cannot be seen. This deceases the correlation coefficient between them.

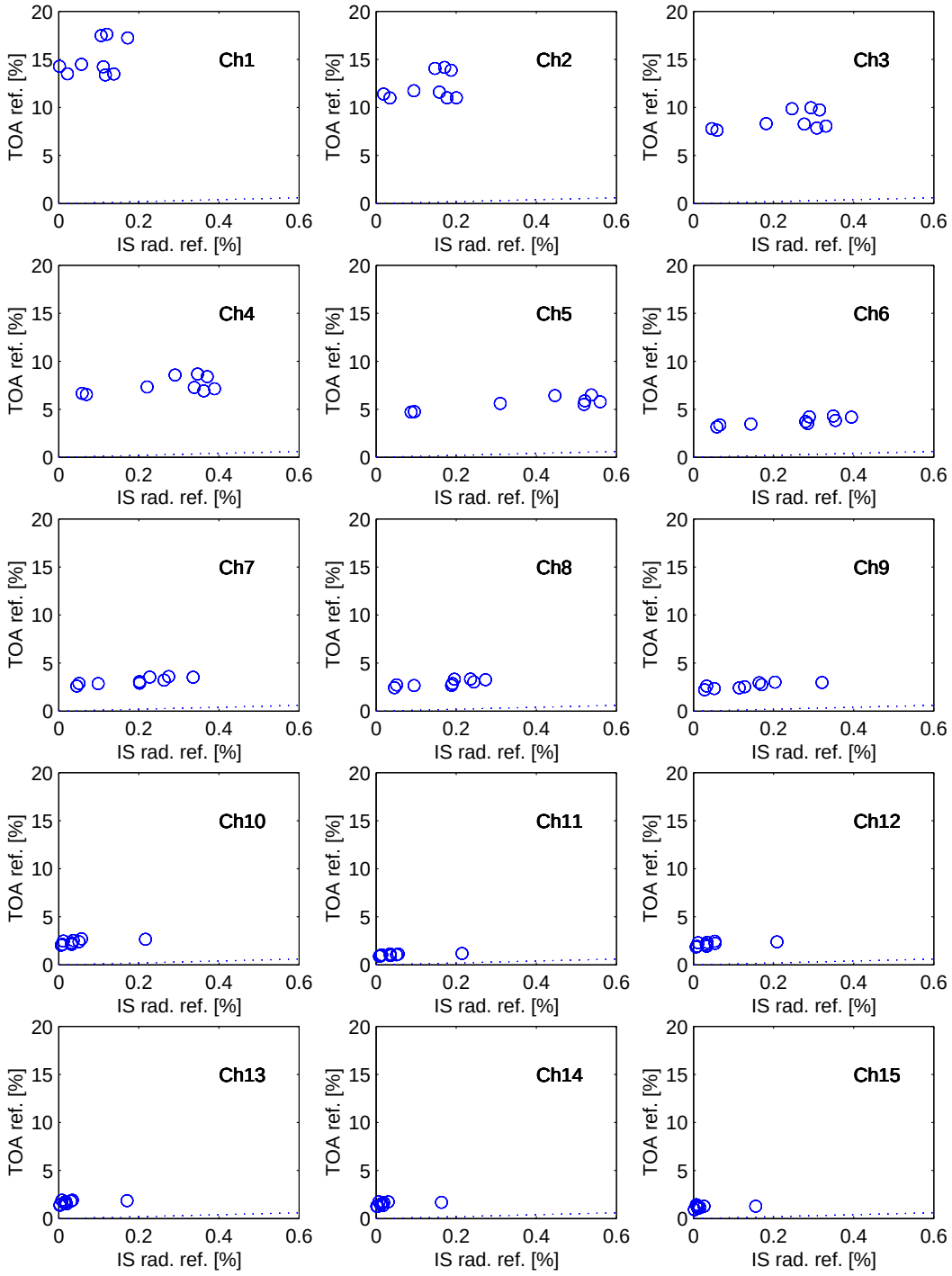

Figure B1: Scatterplots of TOA reflectance and the situ radiance reflectance at all MERIS channels. The in situ radiance reflectances are measured on three days during summer 2007. The TOA radiances are measured on the same three days over the same three locations by MERIS satellite instrument.